UNIVERSITY OF OKLAHOMA

GRADUATE COLLEGE

STATE OF HEALTH ESTIMATION IN LITHIUM-ION BATTERIES USING EXPERIMENTAL AND MODEL DRIVEN APPROACHES

A THESIS

SUBMITTED TO THE GRADUATE FACULTY

in partial fulfillment of the requirements for the

Degree of

MASTER OF SCIENCE

By

LOGAN SCOTT

Norman, Oklahoma

2024

STATE OF HEALTH ESTIMATION IN LITHIUM-ION BATTERIES USING EXPERIMENTAL AND MODEL DRIVEN APPROACHES

A THESIS APPROVED FOR THE
SCHOOL OF AEROSPACE AND MECHANICAL ENGINEERING

BY THE COMMITTEE CONSISTING OF

Dr. Dong Zhang, Chair

Dr. Jie Cai

Dr. Wilson Merchan-Merchan

Table of Contents

List of Figures

List of Acronyms

CC – Constant current charging or discharging of battery.

CCCV – Constant current constant voltage charging or discharging of battery. CCCV uses constant current until reaching a cutoff voltage, which is held constant while reducing the current until reaching a cutoff current.

C-Rate – A rate that defines the current being used for charging or discharging. 1C rate is the current required to charge a battery to 100% capacity in one hour.

DIC – Digital Image Correlation

EHM – Equivalent Hydraulic Model for modelling batteries.

SEI – Solid Electrolyte Interface

SOC – State of charge of a battery, typically defined as the current charge (Ah) divided by the maximum charge (Ah).

SOH – State of health of a battery.

UDDS – Urban dynamometer driving schedule. UDDS schedules are current profiles based on what an electric vehicle would experience, both charging (from regenerative braking) and discharging (driving motors).

Abstract

Meeting the demand for clean, renewable energy in the future will require the use of batteries to meet power demand at times of low supply. Having batteries with a large enough capacity and power output to meet this requirement is imperative, prompting the need for research into estimating the state of health of batteries. This thesis takes two approaches to state of health monitoring: experimental and model driven.

The experimental approach consisted of taking displacement measurements of an LMN-8790140-1C pouch cell using 3D DIC technology. It was determined that there is a strong linear relationship between the displacement of a completely discharged battery and the battery's state of health. It was also determined that there is a potential relationship between displacement, voltage, and state of health. More work needs to be done to verify this relationship. The points that best represented the average displacement were in the middle of the cell or closer to the long sides.

The model driven approach consisted of creating an equivalent hydraulic model to simulate a silicon-graphite composite anode battery. An LG-MJ1 18650 cell was cycled to collect current and voltage data at several different state of health stages. The particle swarm algorithm in MATLAB was used to identify key parameters of the model. Using identified parameters, the model could accurately simulate voltage given a simple current input. The model struggled with simulating a UDDS cycle, but that could be due to poor parameter identification. A relationship was identified between the diffusive time constant of silicon and state of health. More work needs to be done to determine if other state of health indicating parameters, like estimated resistance or the diffusive time constant of the cathode or graphite, can be used in composite anode batteries.

KEYWORDS: State of Health Estimation, GOM Aramis, DIC, Equivalent Hydraulic Model, Composite Anode Batteries

Introduction

The demand for clean, renewable energy is continuing to grow to meet the goal of net-zero carbon emissions in the effort to combat manmade climate change. A prominent challenge preventing the transition to net-zero carbon energy sources is how to meet demand when production is in short supply, e.g. when there is no wind for wind power or no sun for solar power. One strategy of combatting this issue is to use batteries to store excess energy when there is plenty of supply for use when there is little supply. Another area facing challenges towards reaching net-zero carbon emissions is transportation. Electric vehicles have gained considerable traction recently, but some consumers are still hesitant to transition due to range anxiety of low-capacity batteries. A poll by Auto Trader found that fewer than half of UK drivers are willing to make the switch to electric vehicles, with lack of charging stations being a key factor in their willingness. These factors, amongst many others, have prompted the need for research and development of better batteries.

Along with the need for better, longer lasting batteries, is the need to know the useful life left in a battery, or its state of health (SOH). Replacing batteries too soon results in excess cost to consumers, and unnecessary waste if not recycled properly. Replacing batteries too late can cause drastic decreases in charge capacity and performance, potentially causing dangerous situations. Because of these factors, the need for state of health estimation has become a growing field of research.

The most common degradation modes for batteries include Solid Electrolyte Interface (SEI) layer growth, lithium plating, cathode material decomposition, and particle fracture from mechanical stresses (Edge et al.). This thesis studies the effects of mechanical stresses due to the expansion of batteries during cycling and aging using experimental and modelling techniques. Particle fracture can cause both capacity fade (a decrease in the total charge a battery can hold) and power fade (a decrease in the available power of the battery). The experimental approach focuses on the capacity fade and the modelling approach focuses on power fade.

The experimental approach consists of measuring the z-displacement of NMC pouch batteries (LMN-8790140-1C 3.7V 10000 mAh cells) to identify a relationship between state of charge (SOC) and SOH given voltage and displacement measurements. Measuring the internal resistance is a quick method, but only gives an estimate of power fade and not capacity fade.

Charging and discharging the battery completely gives its true capacity but is very time consuming. The goal is to create a relationship that can be used in industry to quickly estimate capacity fade.

The modelling approach consists of developing an equivalent hydraulic model for a silicon-graphite anode battery (LG-MJ1 Cylindrical Cells). With input data, it is easy to identify the capacity of the battery. However, this does not give an idea of the useful power (power fade) over time. The model is used to identify parameters that indicate power fade, such as estimated resistance and diffusive time constant, to potentially identify a relationship between the identified parameters and SOH.

Experimental Approach: SOH Estimation with Z – Deformation Measurements

Background and 3D Digital Image Correlation Theory

The materials used in battery electrodes can undergo multiple phase changes at different lithiation states. These phase changes can cause the overall volume to change considerably while charging or discharging (Leung et al., 2014). Given enough expansion, the materials can develop stress fractures, leading to capacity and power fade (Kwon et al., 2020). Cell expansion is particularly a problem in silicon-anode batteries, which can expand up to 400% (Ai et al., 2022). Multiple studies have used this as motivation for studying the expansion of battery cells during a charge cycle (Leung et al., 2014; Mohtat et al., 2019; Szalai et al, 2022). However, these studies focus on determining high stress areas (Leung et al., 2014), identifying parameters that are SOH indicators (Mohtat et al., 2019), or experimenting with different deformation measurement techniques (Szalai et al, 2022).

Structural decomposition due to phase changes is a commonly accepted degradation mode for batteries. The irreversible reactions in a battery can cause spinel and rock-salt structures to form, which are much more chaotic than the original lattice structure of batteries (Zhuo et al., 2023). As batteries are used over their lifespans, a Solid Electrolyte Interface (SEI) resistive layer develops causing a decrease in capacity and power fade. Likewise, lithium deposits (plating) form on electrode surfaces as battery degrades (Mohtat et al., 2019). All these factors can impact the overall thickness or volume of a battery, suggesting there may be a relationship between the thickness/deformation of a battery and its SOH. Since expansion is dependent on SOC, knowing the SOC at which measurements are taken is a must. However, SOC can be determined by Coulomb counting or estimation from a given open circuit voltage (OCV) curve. This investigation focuses on using displacement measurements along with quickly collectable data, like OCV, to directly predict the SOH of a battery.

Strain gauges are a common method of measuring displacement. However, strain gauges can be very time intensive to install, and measurements can vary depending on where they are placed. Furthermore, strain gauges only measure individual sections of a battery, so getting an accurate picture of displacement over the entire battery is nearly impossible. This study uses 3D digital image correlations (DIC) to generate displacement measurements over the entire surface of the

battery, providing a better visual for displacement across the entire battery. Generating displacement measurements across the whole surface also allows an average measurement to be calculated. The average displacement across the entire surface of the battery may also be more representative since SOC and SOH are bulk properties of a battery.

3D DIC utilizes an artificial speckle pattern or surface irregularities to track coordinates on the surface of a specimen. Images are taken, and an algorithm matches the speckle pattern to the original coordinates of the reference image. Matching the coordinates of images from two cameras allows for a 3D coordinate to be generated. At this point, displacement can be calculated from the difference of the reference coordinates to the new ones. The change in position can also be used for calculating strain, but this was not the focus of this study. More details on the underlying algorithm and DIC can be found in a downloadable white paper from GOM's website (https://www.gom.com/en/topics/digital-image-correlation).

Experimental Procedure

Equipment and Battery Preparation

Battery images were taken using the GOM Aramis 3D Camera system. The assembly consisted of the Aramis Adjustable 800 Camera Frame with two 12M (USB3) cameras and two LED lights (Figure 1). S35 lenses were attached to the cameras for better focusing with a wider field of view. The camera angle came preset from GOM at 25 degrees.

Figure 1: GOM Adjustable Camera Frame with Lights and Cameras from https://www.gom.com/

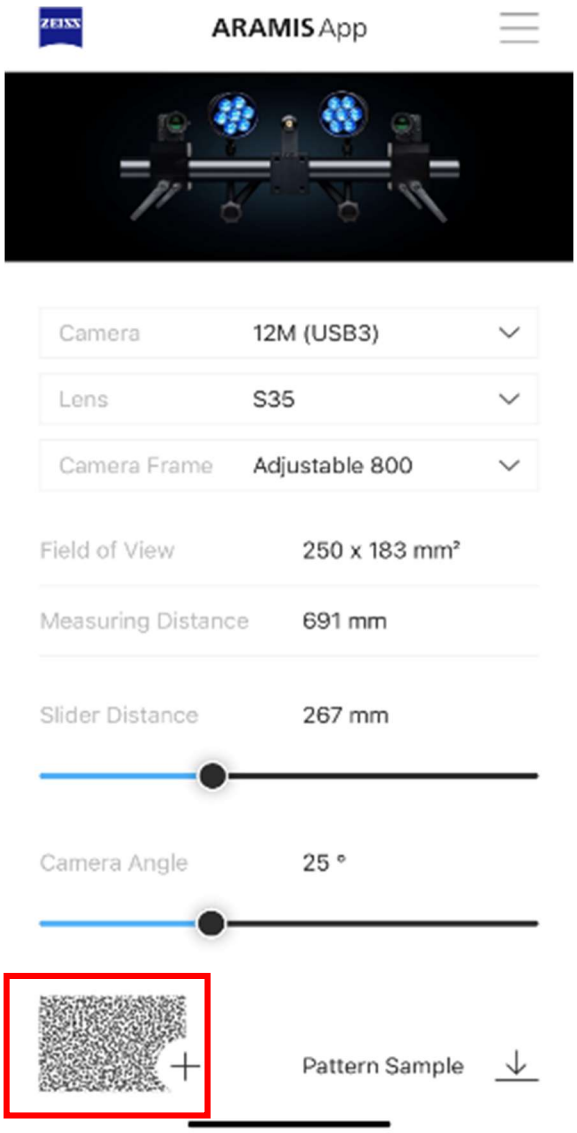

Figure 2: Aramis App Showing Parameters to get the Desired Field of View

A field of view of 250 x 183 mm^2 was selected to fully capture the surface of the battery. The proper slider distance (distance from center point cameras) and measuring distance (from cameras to test object) can be determined by inputting the lens type, desired field of view, and camera angle in the GOM Aramis app (Figure 2). The slider distance for each camera was set to 267 mm. The measuring distance was not measured since the cameras were initially calibrated such that the crosshairs in the computer program would be centered on the laser when at the proper measuring distance for a given slider distance. The lights were oriented to cover the entire surface of the battery. Before each set of measurements, the sensors were calibrated using the ZEISS Inspect Correlate software directions.

The batteries being investigated are LMN-8790140-1C 3.7V 10000 mAh cells. Each battery was glued to a 1/4-inch-thick acrylic plate to ensure a constant, rigid reference surface. The app also provides a recommended spray pattern to get

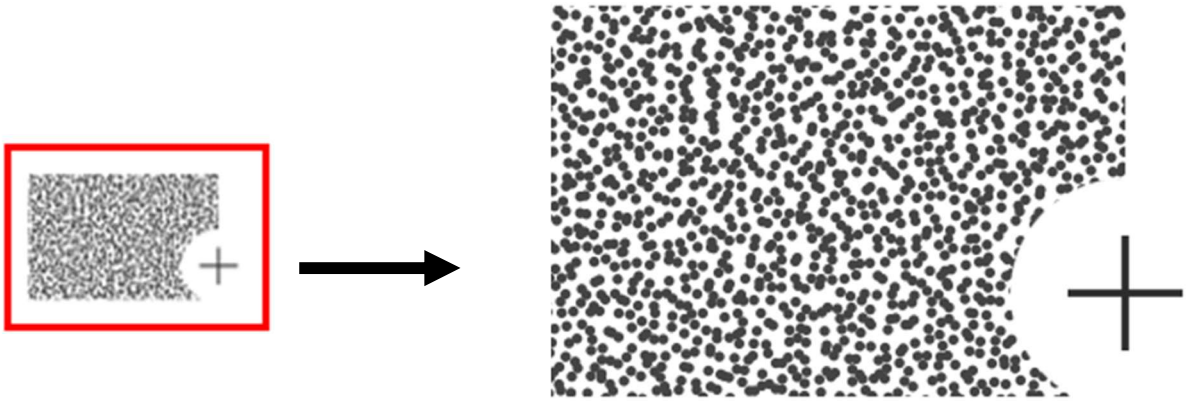

Figure 3: Desired Spray Pattern Generated by Aramis App

the best results (Figure 3). The batteries were initially painted with a flat white spray paint until completely coated. Then, the dot pattern was applied with flat black spray paint by partially pressing the spray button and lightly misting over the battery from approximately 3 feet away. Dot stickers, with a white dot inside a black dot, are attached to the acrylic plate as reference points for the DIC software. A minimum of 5 are recommended by GOM, but more were applied in case some fell off during testing. These reference points make it easier for the DIC software to calculate the position of the battery. The results for each battery are shown in Figures 4, 5, and 6.

Software Configuration

The Digital Image Correlation software being used is the ZEISS Inspection Correlate, which requires a license. Before cycling, a reference image was taken of each battery at 100% SOH, which will be the 0 mm of displacement reference for all future images. A point component, which is used as the $z = 0$ plane, was created by selecting the sticker points on the plate and named "Plate." A local coordinate system was created at the upper left corner of the battery using a 3-2-1-point alignment such that the z-axis is normal to the plate so that z-displacement measures the change in thickness of the cell.

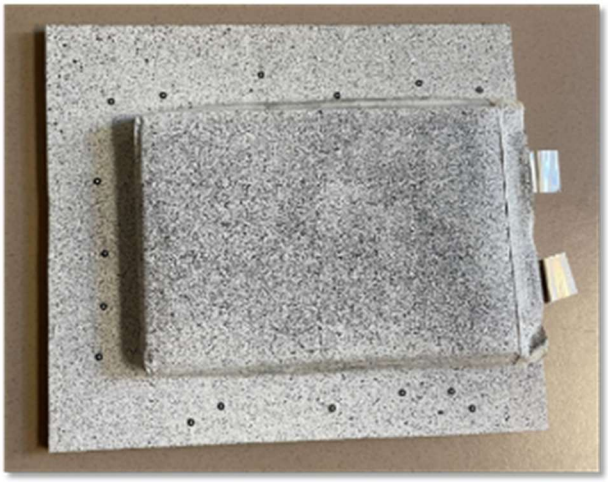

Figure 4: Battery 1 Glued to Plates with Speckle Pattern and Reference Dot Stickers

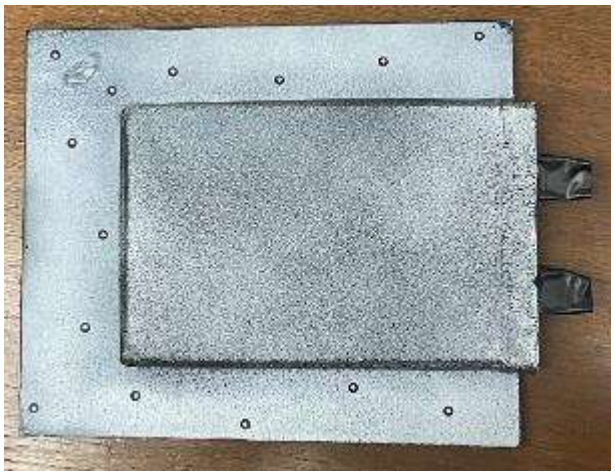

Figure 5: Battery 2 Glued to Plates with Speckle Pattern and Reference Dot Stickers

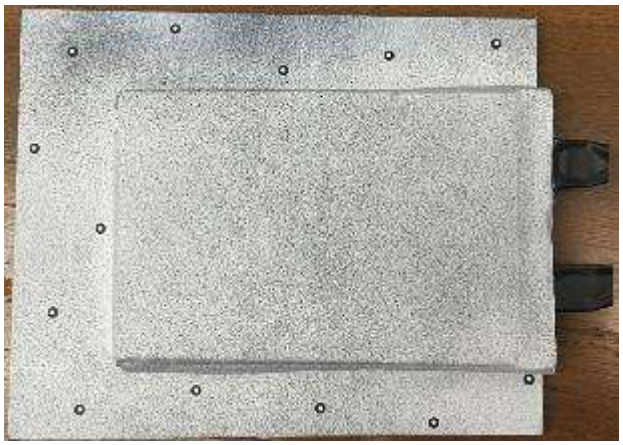

Figure 6: Battey 3 Glued to Plates with Speckle Pattern and Reference Dot Stickers

A Rigid-Body-Motion Compensation was fixed to the “Plate” component to compensate for any movement. Rigid body compensation is important since the battery was being moved between the labs, and other people were using the DIC cameras, so positioning the battery at the exact same position in each picture was impossible. Three images were initially taken with the battery in slightly different positions to ensure the compensation was working properly.

Finally, surface components were created for the faces of the batteries. Two different surfaces were created: one spanning the entire electrode area of the batteries and another excluding a portion of the edges. Having the two surfaces reduces possible measurement errors caused by how the batteries are bound by the casing. A 7x7 grid of surface points was created on each battery, and displacement data was collected at these points. The purpose of the grid is to take a sample on which points most closely match the average and can be used as representative points for when an entire surface cannot be measured.

Data Collection

Before starting each set of measurements, a 0.2C charge current was used in a charge and discharge cycle to measure the charge and discharge capacity of the batteries. Then the batteries were completely discharged using a 0.2C CCCV (see list of acronyms). The cutoff conditions for these are shown in Table 1.

Table 1: Cutoff Conditions for Capacity Check Cycles and Initial Discharging

Battery	Cycle Type	Current (A)	Min. Cutoff Voltage (V)	Max. Cutoff Voltage (V)	Cutoff Current (A)
Capacity Check					
1 (Cycles 146, 186, 226)	CC	2	2.75	4.2	N/A
			Min. CV (V)	Max. CV (V)	
1 (Cycles 66,106)	CCCV	2	2.75	4.2	0.1
2	CCCV	2	2.75	4.2	0.1
3	CCCV	2	2.75	4.2	0.1
Initial Discharge					

All	CCCV	2	2.75	N/A	0.1

Using the charge and discharge capacity, a new 0.2C charge current was estimated. For example, if a battery's capacity was at 9000 mAh, a charge current of 1.8 A would be used instead of 2 A. The currents used for each set of measurements are summarized in Tables 2, 3 and 4. In those tables, the SOH is calculated by dividing the charge capacity of the current cycle by the charge capacity at the beginning of testing, then converting to a percentage. This definition is one definition of SOH typically used to define capacity fade.

$$SOH\% = \frac{Current\ Capacity}{Initial\ Capacity} * 100$$

The charge capacities at cycles 0 and 26 for Battery 1 in Table 2 are based on the cumulative charge during the DIC testing, which is why the SOH at cycle 26 is greater than 100%. After cycle 26, capacity checks were done before DIC measurements.

Table 2: Charge Capacity and Testing Current of each DIC Test for Battery 1

Battery 1			
Cycles	Charge Capacity (Ah)	Testing Charge Current (A)	SOH (%)
0	10.24	2	100%
26	10.95	2	107%
66	9.99	2	98%
106	9.73	1.75	95%
146	9.14	1.9	89%
186	8.52	1.85	83%
226	6.66	1.3	65%

Note that some of the Testing Charge Currents int Table 2 are not 0.2 times the Charge Capacity. This is due to trying to estimate a charge current that would make the cumulative charging time 5 hours by scaling based on the excess time of previous cycles. For example, if the first cycle took 5.5 hours, then the next current would be scaled by $\frac{5}{5.5} = 0.91$.

Table 3: Charge Capacity and Testing Current of each DIC Test for Battery 2

Battery 2			
Cycles	Charge Capacity (Ah)	Testing Charge Current (A)	SOH (%)
5	11.11	2	100%
55	10.92	1.97	99%
105	10.84	1.95	98%
155	10.75	1.94	97%
230	10.64	1.92	96%
280	10.00	1.81	90%
350	9.24	1.67	84%

Table 4: Charge Capacity and Testing Current of each DIC Test for Battery 3

Battery 3			
Cycles	Charge Capacity (Ah)	Testing Charge Current (A)	SOH (%)
5	10.77	2	100%
55	10.49	1.97	98%
105	10.01	1.91	94%
155	9.74	1.81	91%
206	9.6	1.79	90%
256	8.35	1.56	78%

For Battery 1, measurements were taken at SOC of 0%, 20%, 40%, 60%, 80%, and 100% for both the charge and discharge cycles, corresponding to charging the battery at 1-hour intervals to 80%, then charging to the voltage limit of 4.2 V. If the charge time was different than 1 hour, then the discharge from 100% to 80% was adjusted accordingly. Once at 20%, the battery was set to discharge until reaching 2.75 V.

After testing Battery 1, the data showed the hysteresis between the charge and discharge cycle

was small and could be attributed to measurement accuracy/noise of the GOM software. Therefore, to be time efficient, only charging cycle measurements were taken for Battery 2 and Battery 3. The polynomial fit of the Battery 1 data suggested there might be slight decrease in deformation at low SOC. To confirm the slight decrease, and to get more thorough data, measurements were taken at SOC 0%, 5%, 10%, 30%, 70%, and 100% for Batteries 2 and 3, corresponding to charging for 15 minutes, 15 minutes, 1 hour, 2 hours, and charging until the cutoff voltage of 4.2 V was reached.

Note that the previous SOC states are purely nominal. Due to improper charge current estimation, the SOC could be off by as much as 10% (e.g. being at 70% instead of 60%). The difference between intended SOC and actual SOC is accounted for in postprocessing by using the charge and discharge capacity in Ah.

At each SOC for every measurement, the battery was allowed to rest, allowing the voltage to "relax" to an equilibrium. It also allowed the battery to cool if there was an increase in temperature. The resting time depended on the charge time, but in all cases the batteries were given at least 10 minutes. In longer charges, like the 2 hours from 30% to 70%, the batteries were given at least 30 minutes. In addition to letting the batteries rest, temperature measurements were taken with a thermal imaging camera to ensure consistency between deformation measurements. Three images were taken at each measurement to reduce error and measurement uncertainty.

Inducing Aging

After finishing all measurements for a given SOH, the batteries were cycled to induce aging. All cycling was done at 1C current rate (10 A). Battery 1 was cycled using CC from cutoff voltages of 2.75 V to 4.2 V. It was first cycled 26 times and stopped for measurements. Then it was allowed to cycle 40 times between measurements until death (less than 80% SOH). Batteries 2 and 3 were originally cycled with CC from cutoff voltages of 2.75 V to 4.2 V for 50 cycles between measurements. However, Battery 2 was not degrading as rapidly as expected so the charging was changed to CCCV with cutoff current of 0.5C. Using CCCV resulted in greater capacity use and more rapid aging. The cutoff conditions for those charging conditions are summarized in Table 5. The cycles and charging conditions are summarized in Table 6.

Table 5: Charging Cycles to Induce Aging in Batteries

Cycle Type	Current (A)	Min. Voltage / CV (V)	Max. Voltage / CV (V)	Cutoff Current (A)
CC	10	2.75	4.2	N/A
CCCV	10	2.75	4.2	0.1

Table 6: Charging Conditions used for Cycling Batteries at Different Stages

Battery 1								
Cycles	0 – 26	26 – 66	66 – 106	106 – 146	146 – 186	186 – 226		
Cycle Type	CC	CC	CC	CC	CC	CC		
Battery 2								
Cycles	0 – 5	5 – 55	55 – 105	105 – 155	155 – 230	230 – 280	280 – 315*	315 – 350
Charge Condition	CC	CC	CC	CC	CC	CCCV	CC	CCCV
Battery 3								
Cycles	0 – 5	5 – 55	55 – 105	105 – 155	155 – 206	206 – 256		
Charge Condition	CC	CC	CC	CC	CC	CCCV		

* A mistake was made in the charging schedule file for cycling Battery 2 from 280 – 315 cycles, where CC was used instead of CCCV. Using CC resulted in almost no capacity loss from before and after. Battery 2 was then cycled with CCCV from 315 – 350 cycles. Since the purpose of cycling was simply to age the batteries, this mistake has no effect on measurements.

Results and Discussion

Z – Displacement relationships

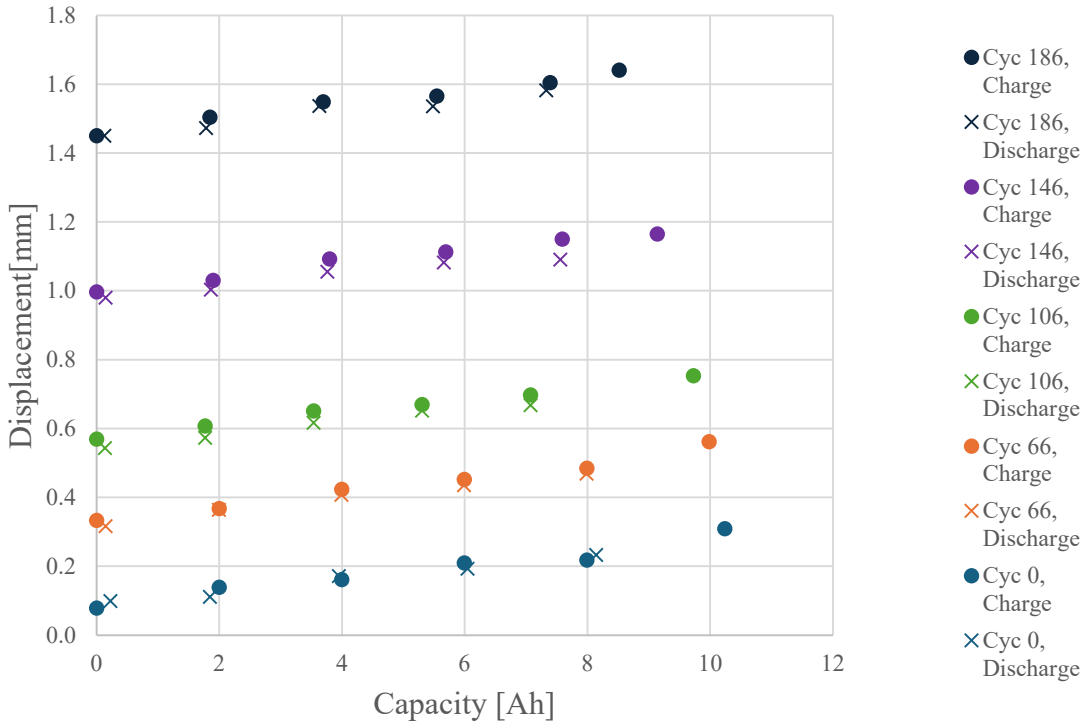

Figure 7: Average Displacement vs. Capacity of Battery 1 for Charging and Discharging at Various SOH Stages

Figure 7 shows the data from Battery 1 for the average z-displacement across the battery surface vs the capacity of the battery. The capacity was determined by adding the capacity charged during every 20% SOC increment, or subtracting the capacity discharged. It shows that the measurements align well between charging and discharging at various SOH stages. The gap at 80% SOC between the charge and discharge curve after 146 cycles is 0.06 mm. The difference can likely be attributed to the tolerance of the Aramis cameras and GOM software. Otherwise, there appears to be negligible hysteresis between the displacement measurements for charging and discharging at the same SOC. This suggests that data analysis does not require knowledge of if a battery was charged or discharged before measurements, making data collection and analysis simpler.

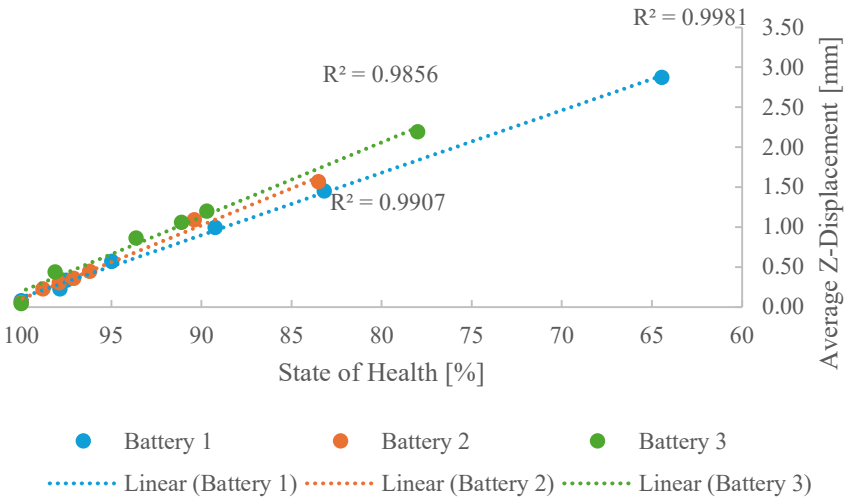

Figure 8: Average Z-Displacement vs State of Health at 0% SOC for Each Battery

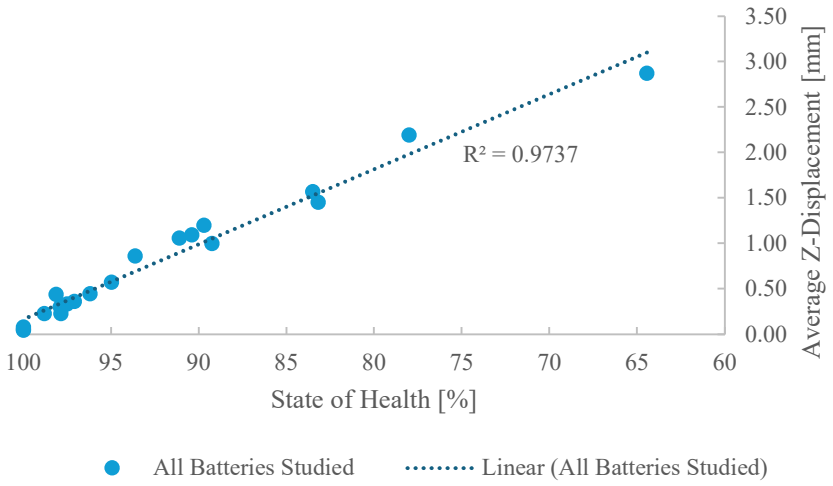

Figure 9: Average Z-Displacement vs State of Health at 0% SOC for All Batteries

Figure 8 shows the plots of the Average Z-Displacement vs State of Health at 0% SOC for each of the three batteries experimented with. Note that 100% SOH and decreases moving right along the x-axis. It shows the linear trendlines for each battery. The minimum R^2 value of the three plots is 0.9856, suggesting there is a significant linear relationship between the average z-displacement and the state of health of a battery. Figure 9 shows the combined trendline for all three batteries. The R^2 value of the combined trendline is 0.9737, so there is still a strong linear relationship between the average z-displacement and the state of health of a battery. This suggests that when given the z-displacement of a battery after it has been completely discharged, the state of health of the battery can be estimated.

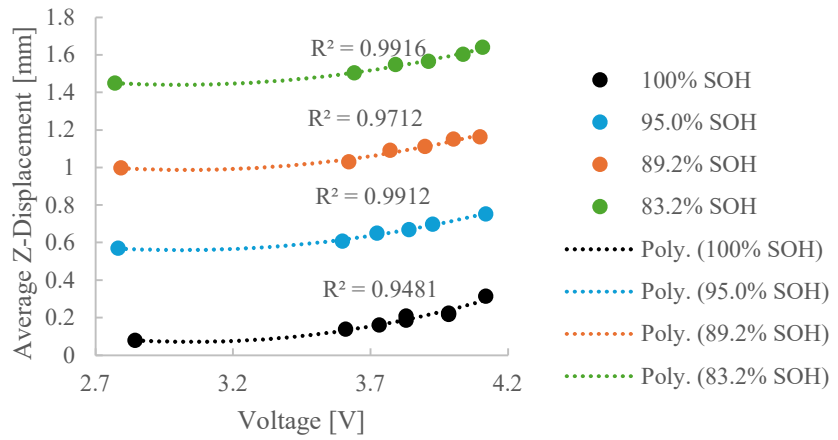

Figure 10: Average Z-Displacement vs Voltage of Battery 1at Various State of Health Stages

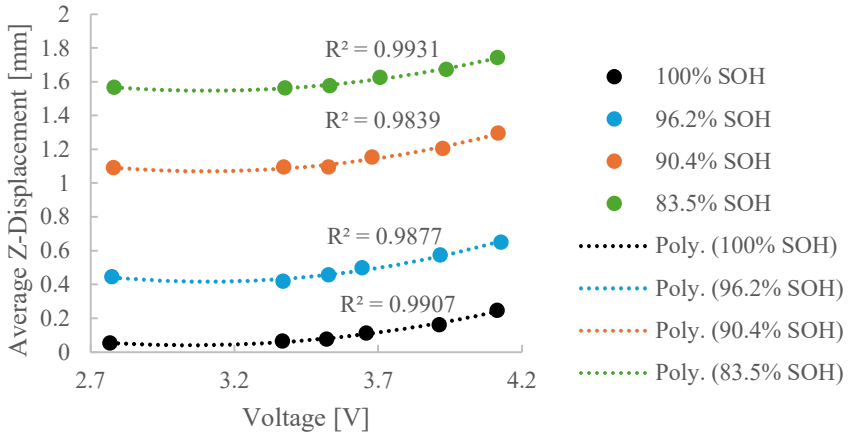

Figure 11: Average Z-Displacement vs Voltage of Battery 2 at Various State of Health Stages

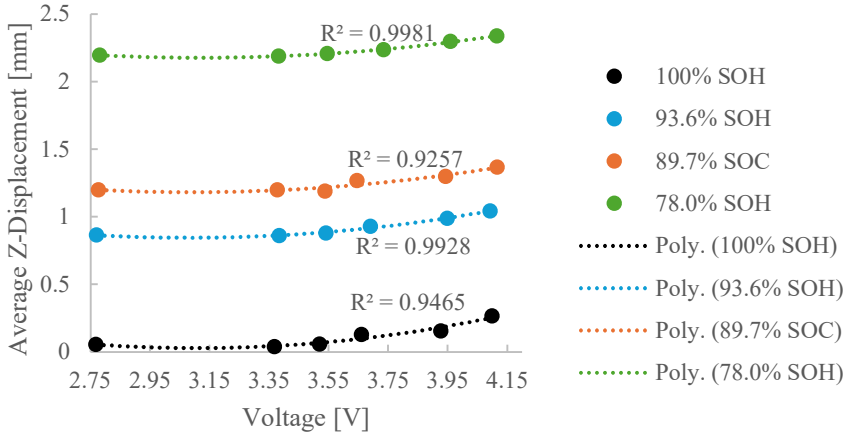

Figure 12: Average Z-Displacement vs Voltage of Battery 3 at Various State of Health Stages

Figures 10, 11, and 12 show plots of average z-displacement vs voltage at several SOH stages for the different batteries. A second order polynomial fit for each of the SOH curves results in high R^2 values, with the lowest being 0.9257, signifying there is some relationship between voltage and average z-displacement at various SOH stages. That is, given a voltage and displacement value, it may be possible to recover the SOH. More work is needed to confirm this hypothesis.

Representative Points of Average Displacement

The 7x7 grid was created by placing the evenly dividing the battery surface in each direction. There were 7 lines created in each direction, starting with a line on one edge and ending with a line on the opposite edge in the respective direction. Points were placed at the intersections of these lines. Points were numbered with two digits, with the first digit being the vertical line it lies on from left to right and the second digit being the horizontal line it lies on from top to bottom. For example, the top left corner is Point 11, the bottom left corner is Point 17, the top right corner is Point 71, and the bottom right corner is Point 77. Figure 13 shows a sample image of a 7x7 grid that was created.

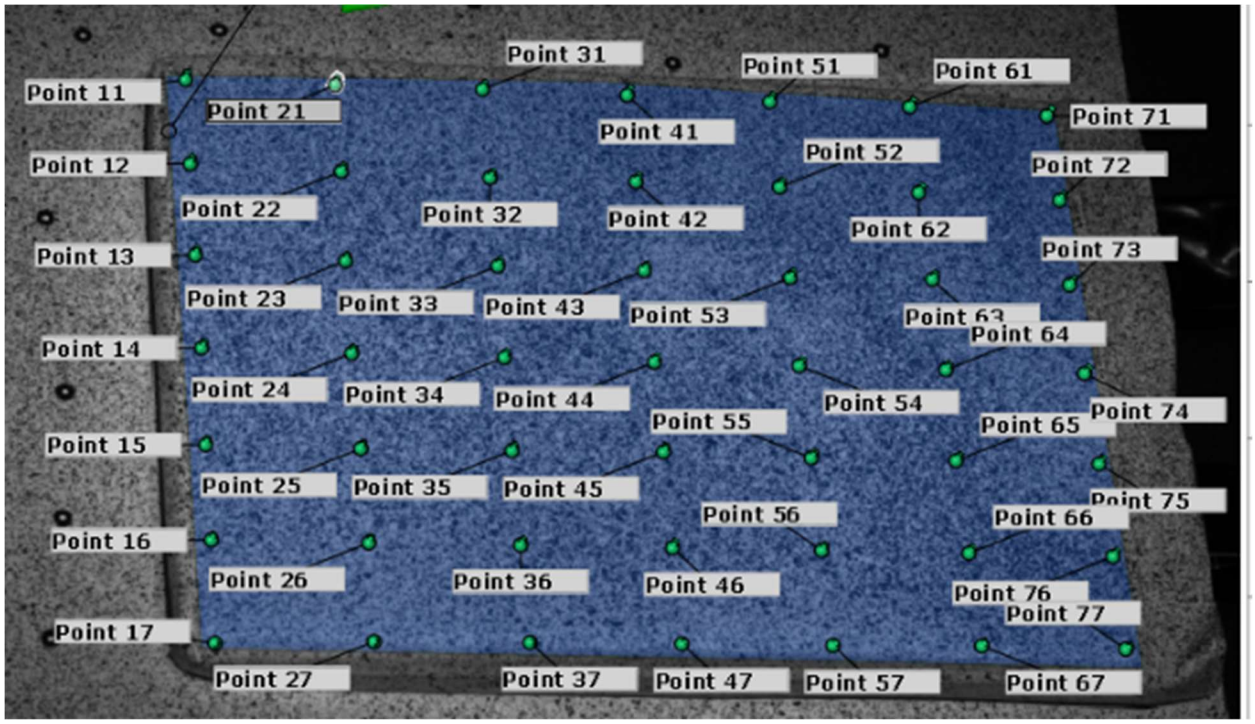

Figure 13: 7x7 Grid of Points on Battery 1

Table 7 below shows the five best points that minimize the error over all measurements between the displacement at that point and the average z-displacement.

Table 7: 5 Best Points to Minimize RMSE of Each Battery

Battery 1							
No Edges	RMSE	Point	Point 32	Point 33	Point 42	Point 52	Point 62
		Value	0.010	0.018	0.017	0.012	0.009
Battery 4							
No Edges	RMSE	Point	Point 33	Point 34	Point 35	Point 36	Point 42
		Value	0.067	0.061	0.035	0.024	0.035
Battery 5							
No Edges	RMSE	Point	Point 25	Point 32	Point 35	Point 42	Point 46
		Value	0.090	0.117	0.110	0.094	0.112

In general, the best points compared to the average without the edge appear to be on the third vertical line (points with 3 as the first digit) and on the second, fifth, or sixth horizontal line. The best points compared to the averages without the edge are shown in Figures 14, 15 and 16. In these figures, the red corresponds to areas of large displacement and blue corresponds to areas of low displacement. Each image is scaled by the values in the image to accentuate the high and low spots. The values for each point and the average for the frame are listed. All images are at 0% SOC around 90% SOH to show the similarities between batteries at similar stages.

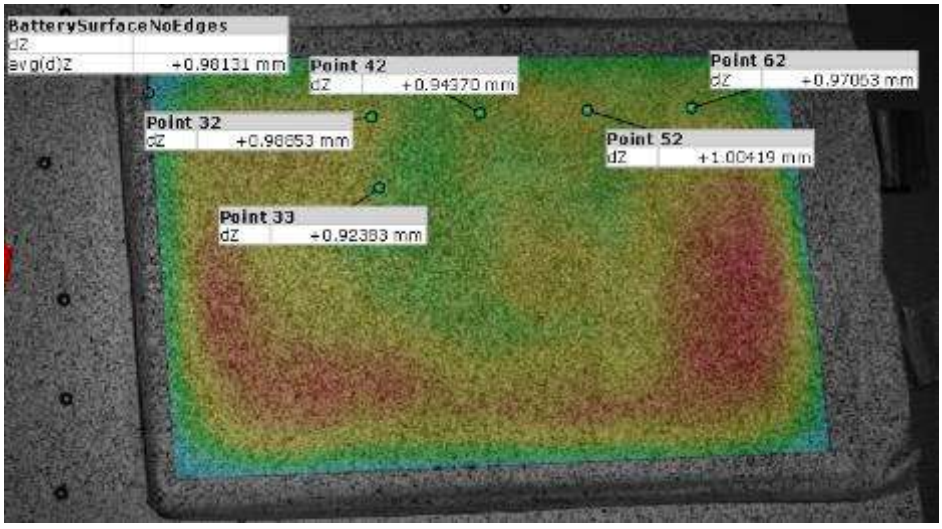

Figure 14: Battery 1 Displacement Map Showing Best Points by RMSE of Average Without Edges at 0% SOC After 146 Cycles)

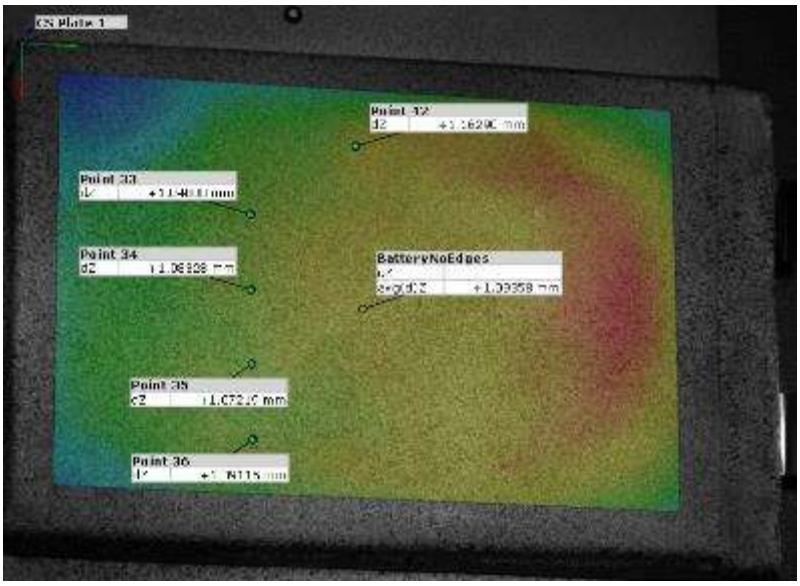

Figure 15: Battery 2 Displacement Map Showing Best Points by RMSE of Average with No Edges at 0% SOC After 281 Cycles

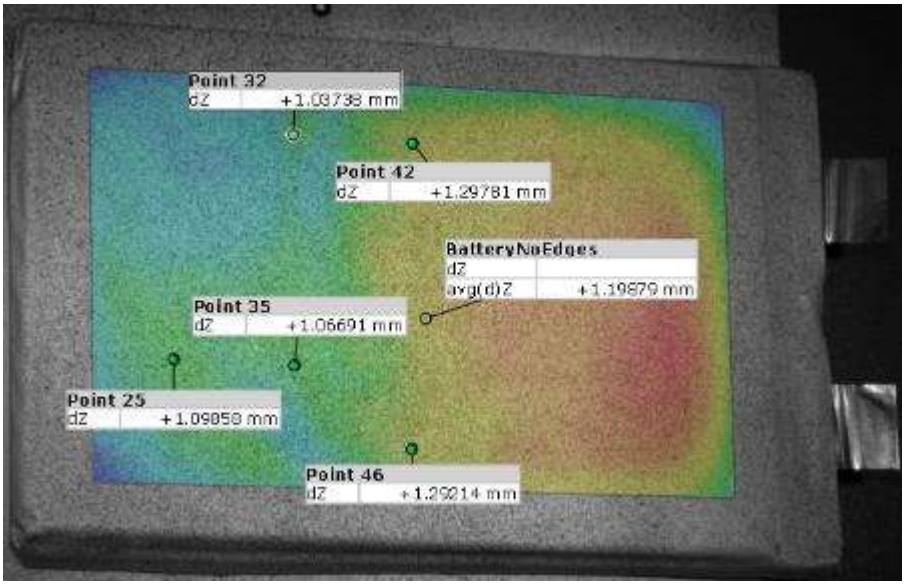

Figure 16: Battery 3 Displacement Map Showing Best Points by RMSE of Average with No Edges at 0% SOC After 206 Cycles

Nonuniform Displacement Between Batteries

Figures 14, 15, and 16 show that there are high displacement areas by the electrode tabs. Figure 14 shows a "ring" of high areas forms around the edges of the battery. Figure 14 shows that the best points tend to stay on this ring, but this is not as true in Figures 15 and 16. In fact, the best points do not show much consistency between batteries. Figures 17, 18, and 19 show the batteries closer to 95% SOH, where the differences in high displacement areas are more pronounced.

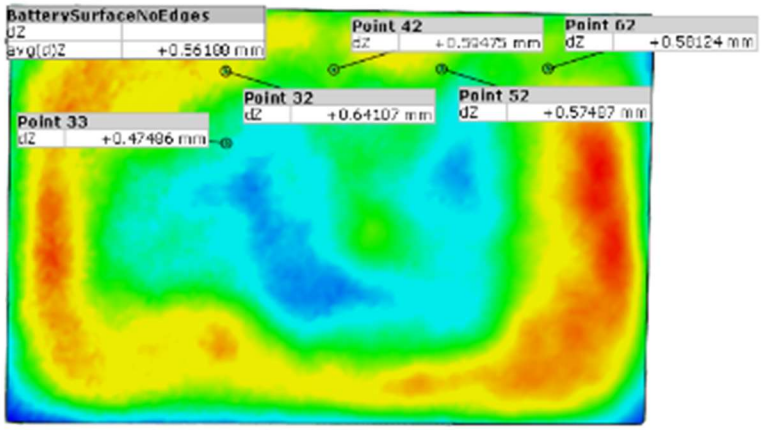

Figure 17: Battery 1 Edge Effect at 0% SOC After 106 Cycles (95% SOH)

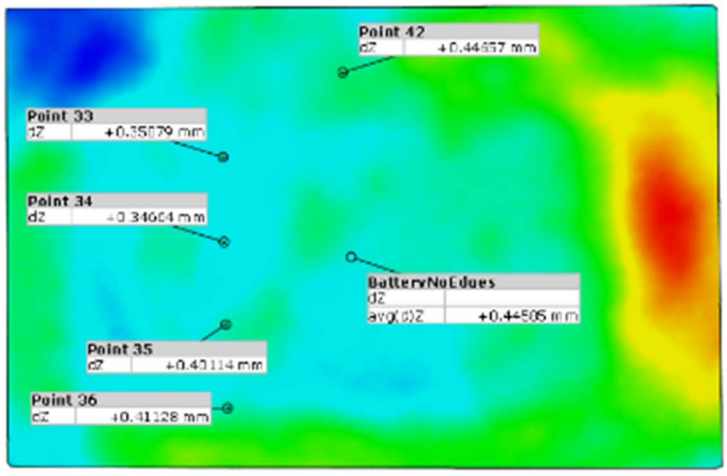

Figure 18: Battery 2 Edge Effect at 0% SOC After 230 Cycles (96% SOH)

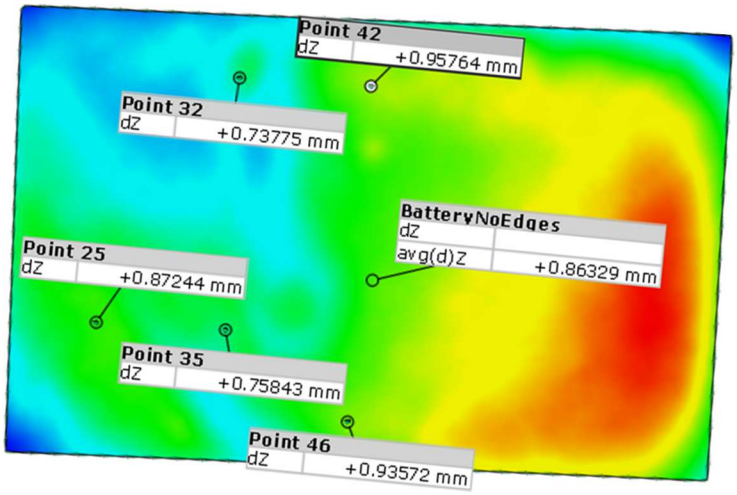

Figure 19: Battery 2 Edge Effect at 0% SOC After 105 Cycles (94% SOH)

In Battery 1, there is a ring of high displacement around the edges of the battery. In Battery 2, the area of high displacement is the right edge close to the electrode tabs. In Battery 3, the high displacement is the bottom right corner with some greater displacement in the bottom left corner. This suggests that the displacement is not uniform between different batteries. So, even though there is a strong relationship between average displacement and SOH, nonuniformity of displacement makes SOH estimation difficult in practice where only a handful of points are measured. More work is needed to determine where displacement sensors should be placed in practice for the best results.

Follow-On Work

The biggest area remaining for follow-on work is to determine a relationship between displacement, voltage, and SOH. A relationship between these variables will be found by regression machine learning models, such as support vector machine (SVM) regression, using the voltage and displacement as inputs and SOH as an output. Data sets from Batteries 1 and 2 can be used as the training data, with the data from Battery 3 being used for validation, or any other combination like of two data sets for training and another for validation.

The other area for follow-on work is to replicate real-life conditions for industrial SOH estimation as well as battery use. The goal of using displacement for SOH estimation is to decrease the time and expense for testing batteries. Using DIC methods is impractical for real-

life application, but displacement sensors can be used. More work needs to be done to determine the optimal placement of these displacement sensors. Additionally, the batteries tested were kept in a controlled environment with limited temperature variation and mechanical stresses. Follow-on work can include subjecting batteries to conditions batteries an electric vehicle would experience, like extreme temperatures or vibrations, to see if degradation relationships still hold.

Conclusion

Using the Aramis cameras and the GOM Inspect Correlate Software, measurements were taken for the Z-Displacement of three LMN-8790140-1C batteries. It was confirmed that the batteries expand as they are charged and contract as they are discharged. There was almost no hysteresis between displacement measurements between charging and discharging, and any hysteresis could likely be attributed to measurement tolerance.

As the batteries aged, the displacement at 0% SOC increased. It was determined that there is a strong linear relationship between the displacement at 0% SOC and the SOH of the battery. More work could be done to validate this hypothesis by taking displacement measurements at 0% SOC, estimating the SOH from those measurements and a linear model, and comparing to what the actual SOH is. Another relationship was discovered between displacement and voltage measurements at various SOH stages, suggesting that voltage and displacement measurements could potentially be used to extract the state of health. More work is needed to determine if voltage and displacement measurements alone can be used to reliably estimate SOH. The plan for future work is to use machine learning to create and validate a model to estimate SOH given displacement and voltage.

A 7x7 grid of points was created on the surface of each battery. The points that minimized the RMSE to the average displacement varied between each battery, but they tended to be in the middle of the battery, or along the on the sides just off the top or bottom edges. More work is needed for finding representative points that can be used for quick SOH estimation in industrial practice.

Model-Driven Approach: SOH Estimation on Si-Gr Anode Batteries

Background

A promising material for future batteries that require high storage capacity is silicon. Silicon has a theoretical capacity of 4200 mAh/g, whereas graphite only has a capacity of 375 mAh/g (Kwon et al., 2020). For the same weight of material, silicon can store over 10 times that of graphite. Silicon is also very abundant, with some estimates saying it makes up 27.7% of Earth's crust by mass (Royal Society of Chemistry, 2024). Silicon's large specific capacity and natural abundance makes it ideal for applications requiring a large capacity, like grid storage, or added capacity with minimal weight, like electric planes and cars.

Although it is a promising material, silicon has some issues, especially regarding lifespan. Silicon can theoretically expand up to 400% over a charging cycle (Ai et al., 2022). The excessive expansion causes silicon anode batteries to develop stress fractures, leading to capacity and power fade (Kwon et al., 2020). Zhu et al. (2019) found that a silicon only battery's capacity degraded from 2467.6 to 1522 mAh/g in 500 cycles (61.7% SOH). A way to combat the problem of short lifespans is to use additives and create a composite anode material. Zhu et al. (2019) used Dimethylacrylamide (DMAA) as an additive. With 2.5% DMAA, the capacity degraded from 2467.6 to 1950.7 mAh/g in 500 cycles (79% SOH). (Kwon et al., 2020) used a silicon-graphite composite material stabilized with corn starch, which resulted in 80% SOH capacity retention over the same 500 cycles.

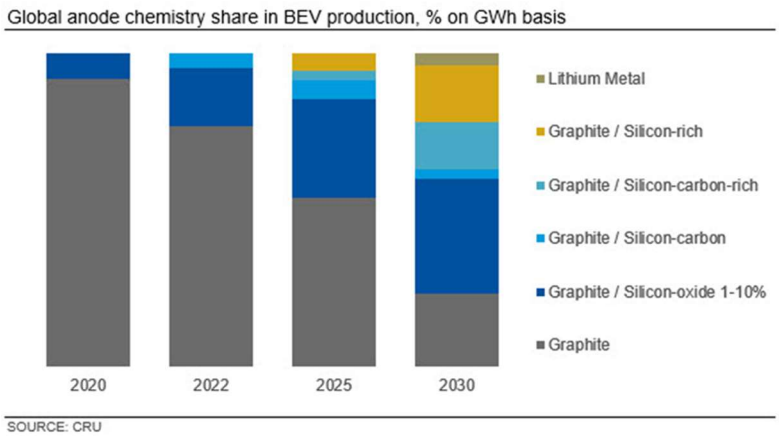

Figure 20: Expected Global Anode Chemistry Share Until 2030 (Adham et al. 2023)

Due to the high capacity and ability to increase useful life, silicon-graphite composites are expected to become the most prevalent anode material. Figure 20 shows the expected global anode chemistry distribution over the 6 years, as predicted by Adham et al. (2023).

Another advantage of silicon-graphite composites is that "silicon-based technologies are compatible with the manufacturing processes of conventional lithium-ion cells" (Adham et al.,

2023). For its expected prevalence, silicon-graphite is the composite anode material of interest for modelling. One challenge in modelling silicon or silicon composite batteries is the hysteresis of the open circuit potential (OCP) curve of silicon between charging and discharging (Figure 21). A successful model will be able to accurately simulate the open circuit voltage (OCV) of a battery cell during charging and discharging, as well as rapid jumping between charging and discharging like an electric vehicle would be subject to.

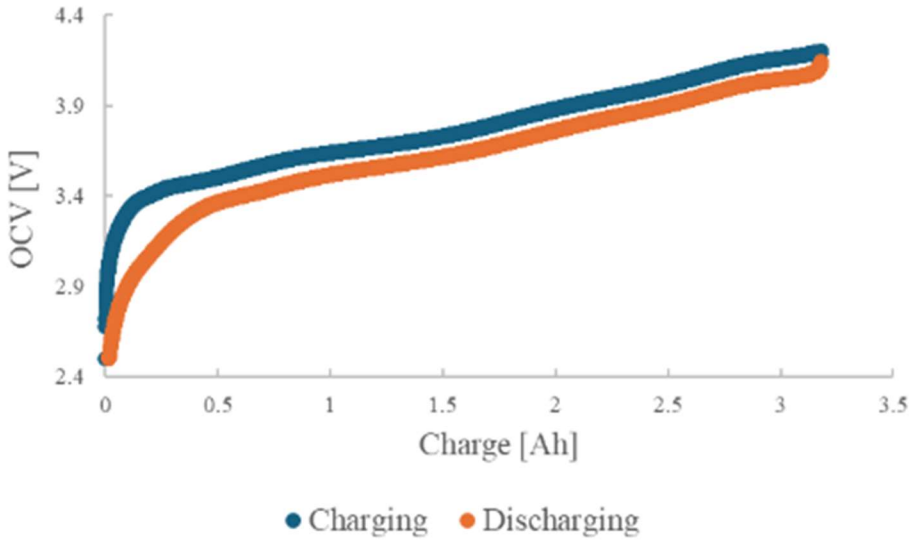

Figure 21: OCV Curve of LG-MJ1 Cell Showing Hysteresis Between Charging and Discharging

The most complete electrochemical model for batteries is the Doyle-Fuller-Newman (DFN) model. The DFN model is a system of nonlinear partial differential equations that capture solid state and electrolyte diffusion dynamics and electric potentials of a battery cell (Xia et al., 2017). Moura et al. (2017) summarized the model as a "mathematical structure, which contains linear PDEs, quasi-linear PDEs, ODEs in space and nonlinear algebraic constraints." Due to its complexity, solving the DFN model is time consuming and computationally expensive. Zülke et al. (2021) claimed that "the recent development of linear scaling algorithms, with compiled language and cloud-based data management to solve the DFN model" makes the DFN much more manageable. However, not all applications may have cloud resources, and it may still not be fast enough for real time controls application.

The single particle model (SPM) simplifies the DFN model through some assumptions. These assumptions and SPM model development can be found from several sources, such as Moura et al. (2017). As the name suggests, the SPM model reduces each electrode of the DFN model to

one particle. It has a “significantly simplified structure,” since the dynamical equations are “linear and quasi-linear PDEs” (Moura et al). Although it is much simpler, solving PDEs are still time consuming and may still not be fast enough for real time controls application.

The equivalent circuit model (ECM) is perhaps the simplest model for batteries. It models a battery as a circuit, consisting of the OCV source, with a resistor-capacitor pair in series with another resistor (Figure 22). The ECM is modeled as a linear system of ODEs, which can be solved quickly with proper methods. However, due to its simplicity, it is difficult to capture the hysteresis between charging and discharging. Additionally, “due to the lack of electrochemical meaning, charge-control policies based on ECMs cannot take explicitly into account the occurrence of degradation phenomena” (Goldar et al., 2020, p. 2).

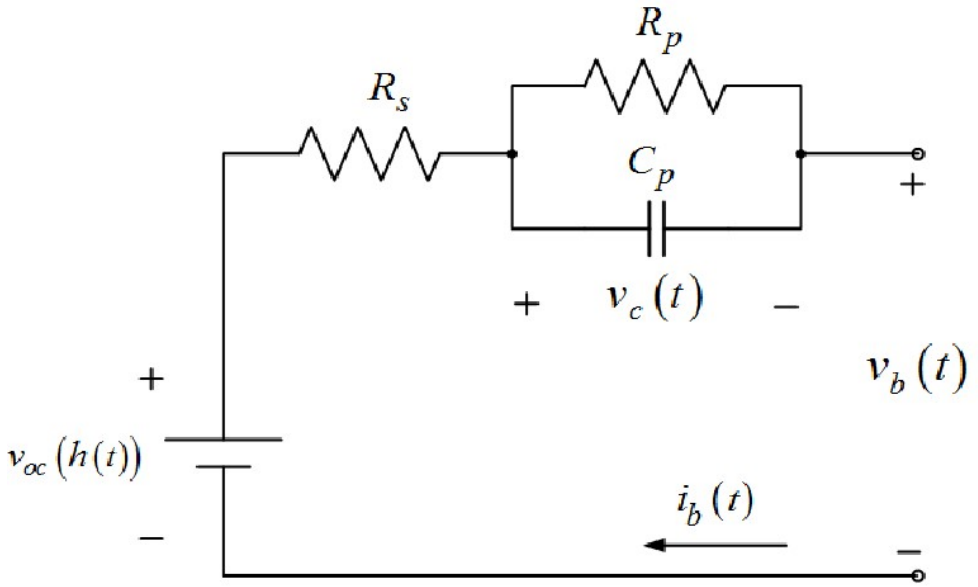

Figure 22: Schematic of a First Order Equivalent Circuit Model (Mu et al., 2013)

The equivalent hydraulic model (EHM) is a linear model formed by taking a second order Padé approximation of the SPM model (Couto et al., 2016, Part I). The EHM has the benefit of being a linear ODE model, which is easy for solvers to calculate, while keeping an electrochemical meaning. Since the model parameters still have an electrochemical meaning, these parameters can be determined through proper experimental methods or found from available literature, allowing for better fitting models and greater potential for SOH identification. A drawback for the EHM model is that it may not be accurate for high charge rates. Gao et al. (2023) observed that a Pseudo 2-Dimensional model (P2D) has “large voltage prediction error… with

0.5C/1C/1.5C discharge at low SOC range" (p. 2). Since the EHM model approximates the SPM model, which is a simpler version of the P2D model, it would follow that the EHM model would struggle with high C rates. Further details of the equivalent hydraulic model are discussed in the "**Theory** – *Equivalent Hydraulic Model*" section.

The goal of this research is to create a model that can accurately simulate charging cycles on a silicon-graphite battery, including being able to identify key parameters of the model. Ai et al., (2022) have already done work in developing a successful composite anode model for LG M50 cells. Creating a model that works with the LG-MJ1 cells possessed by the research group will lay the groundwork for future projects like optimal controls or real time monitoring. Another goal for modelling is to identify key parameters for SOH indication. Prasad and Rahn (2013) found that two parameters, estimated resistance and diffusive time constant, can potentially be used as SOH indicators. However, they model a battery cell with a single material anode. This research will seek to determine if resistance and/or diffusive time constant can be used as SOH indicators in a composite anode battery.

Theory

Equivalent Hydraulic Model Development

The equivalent hydraulic model equates each particle of the SPM model (each electrode) as a system of two hydraulic tanks (Figure 23). In the case of a silicon-graphite anode, each material is given its own dynamics. Each particle has two states: surface concentration (CSC, Tank 1 of Figure 23) and bulk concentration (SOC, Tank 2 of Figure 23). The following derivation summarizes the EHM model as presented by Couto et al. (2016, Part I).

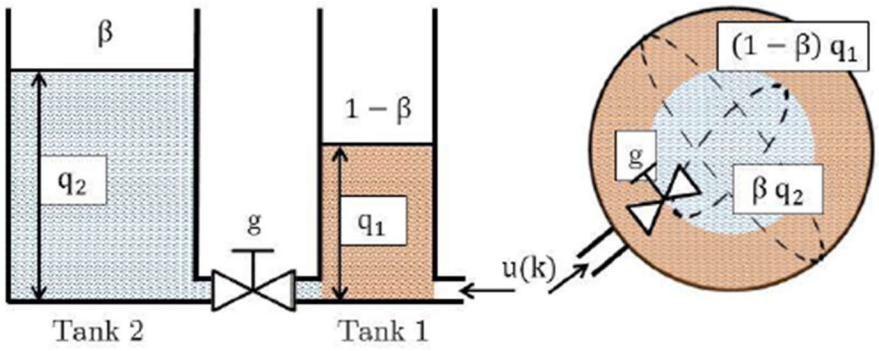

Figure 23: Diagram Equating a Battery Particle as Two Hydraulic Tanks, Courtesy of Couto et al., 2016, Part I

The tanks' dynamics can be described by the following equations.

$$(1-\beta)\dot{q_1} = \big(q_2(t) - q_1(t)\big)g + u(t)$$

$$\beta\dot{q_2} = \big(\mathrm{q_1(t) - q_2(t)}\big)\mathrm{g}$$

In the above equations, $1-\beta$ and β are each cross-sectional area of the two tanks, q_1 and q_2 are the height of each tank, g is some constant rate the tanks exchange lithium, and $u(t)$ is some input current at time t (Couto et al., 2016, Part I). These dynamics are then linked to the electrode dynamics by

$$SOC(t) = (1-\beta)q_1(\mathrm{t}) + \beta q_2(t)$$

$$\mathrm{CSC} = \mathrm{q_2}(t)$$

Where $\beta \in [0,1]$ is the ratio of core volume to the sphere to the total volume. Using the second order Padé approximation of the SPM model and equating it to the above dynamics, gives

$$g = \frac{147}{20}\frac{1}{\tau} \quad , \quad \beta = \frac{7}{10}$$

Where τ is the diffusive time constant of the electrode material. The time constant is defined as

$$\tau = \frac{R^2}{D}$$

Where R is the particle radius (typically provided by manufacturer) and D is the diffusivity of the particle. Using variables $x_1 = SOC$ and $x_2 = CSC$, the dynamics discretized in time of each electrode component can be described by

$$f_1(x(t), u(t)) = -\mathrm{u(t)}\Delta t \qquad \text{Eq. 1}$$

$$f_2(x(t), u(t)) = \frac{\mathrm{g}\Delta t}{\beta(1-\beta)}\mathrm{x_1(t)} - \frac{\mathrm{g}\Delta t}{\beta(1-\beta)}\mathrm{x_2(t)} + \frac{\mathrm{u(t)}\Delta t}{(1-\beta)} \qquad \text{Eq. 2}$$

Where the input $\mathrm{u(t)}$ is the interfacial current density of each electrode (this will later be referenced as j). The dynamics can be used to find the states at the next time step by

$$x_1(t+1) = \mathrm{x_1(t)} - \mathrm{u(t)} \qquad \text{Eq. 3}$$

$$x_2(t+1) = \frac{\mathrm{g}}{\beta(1-\beta)}\mathrm{x_1(t)} + \left(1 - \frac{\mathrm{g}}{\beta(1-\beta)}\right)\mathrm{x_2(t)} + \frac{\mathrm{u(t)}}{(1-\beta)} \qquad \text{Eq. 4}$$

The output of the EHM model is the voltage of the battery cell. Voltage is a function of the OCP of each electrode, overpotentials, and internal impedance (Speltino et al., 2013).

$$V = \eta_p + \phi_p\left(CSC_p\right) - \eta_n - \phi_n(CSC_n) - K_r\frac{j}{A} \qquad \text{Eq. 5}$$

In Equation 5, $\phi_p\left(CSC_p\right)$ is the OCP of the positive electrode as a function of the surface concentration of the cathode and $\phi_n(CSC_n)$ is the OCP of the negative electrode as a function of the surface concentration of the anode. OCP curves can be determined through experiments, or found in literature for common materials. K_r is a resistance term incorporating other resistance terms, j is the interfacial current, and A is the interfacial area of the electrodes. The terms η_p and η_n are the overpotentials of the cathode and anode, respectively.

Overpotential is calculated via the Butler-Volmer dynamics (Ai et al., 2022).

$$\eta = \frac{RT_{ref}}{0.5F}\sinh^{-1}\left(\frac{j}{2a_s i_0}\right) \qquad \text{Eq. 6}$$

Where R is the ideal gas constant, T_{ref} is the ambient temperature in Kelvin, F is Faraday's constant, a_s is the surface to volume ratio of each component, and i_0 is the exchange current density. The surface to volume ratio of each component is given by

$$a_s = \frac{3V_s\epsilon_s}{R_s}$$

Where V_s is the volume fraction of each material in its respective electrode, ϵ_s is the volume of active material, and R_s is the particle radius (Ai et al.) Different definitions exist for the exchange current density, but the one given by Couto et al. (2016, Part 1) is

$$i_0 = \mathrm{kC_{max}}\sqrt{C_e}\sqrt{CSC(1-CSC)} \qquad \text{Eq. 7}$$

Where k is the charge transfer reaction rate, C_{max} is the maximum lithium concentration of each component, and $\overline{C_e}$ is the average lithium concentration in the electrolyte phase. Note that $\overline{C_e}$ is the only reference to the electrolyte phase – in the SPM and EHM models the electrolyte dynamics are ignored.

The presence of silicon complicates the system. For composite electrodes, the two materials are often treated like resistors in parallel. This approach has been taken by Bartlett et al. (2016) to model a composite cathode and Ai et al. (2022) to model a silicon-graphite anode. In a parallel resistor pair, the voltage across each resistor. In the context of silicon and graphite, the voltage of each should be the same at any moment in time (under steady state/equilibrium assumptions).

$$V_{Si} = V_{gr}$$

$$\eta_{si} + \phi_{si}(CSC_{si}) = \eta_{gr} + \phi_{gr}(CSC_{gr}) \quad \text{Eq. 8}$$

Parallel resistors also follow Kirchoff's current law, which states the current into or out of the pair is equal to the sum of currents through each resistor. In the context of silicon and graphite, the total interfacial current density j (which is the interfacial current density of the cathode j_p) is equal to the interfacial current density in the silicon j_{si} plus the interfacial current density in the graphite j_{gr}.

$$j = j_p = j_{si} + j_{gr} \quad \text{Eq. 9}$$

To summarize, there are six states with linear dynamics, two algebraic equations, and a nonlinear output equation. These equations form a system of differential algebraic equations (DAEs), which can be solved in MATLAB with the ODE15 function when the DAEs are of the form

$$y' = f(t, y, z)$$

$$0 = g(t, y, z)$$

The output of Equation 5 is not needed to solve the system of DAEs. The following are all the equations for the MATLAB function to simulate the EHM. The states will be defined as $x_1 = SOC$ and $x_2 = CSC$ in the cathode, $x_3 = SOC$ and $x_4 = CSC$ in graphite, and $x_5 = SOC$ and $x_6 = CSC$ in the silicon.

$$x_1' = -j_p$$

$$x_2' = \frac{\mathrm{g}}{\beta(1-\beta)}\mathrm{x_1(t)} - \frac{\mathrm{g}}{\beta(1-\beta)}\mathrm{x_2(t)} + \frac{\mathrm{j_p}}{(1-\beta)}$$

$$x_3' = -j_{gr}$$

$$x_4' = \frac{\mathrm{g}}{\beta(1-\beta)}\mathrm{x_3(t)} - \frac{\mathrm{g}}{\beta(1-\beta)}\mathrm{x_4(t)} + \frac{\mathrm{j_{gr}}}{(1-\beta)}$$

$$x_5' = -j_{si}$$

$$x_6' = \frac{\mathrm{g}}{\beta(1-\beta)}\mathrm{x_5(t)} - \frac{\mathrm{g}}{\beta(1-\beta)}\mathrm{x_6(t)} + \frac{\mathrm{j_{si}}}{(1-\beta)}$$

$$0 = j_p - j_{si} - j_{gr}$$

$$0 = \eta_{si} + \phi_{si}(CSC_{si}) - \eta_{gr} - \phi_{gr}(CSC_{gr})$$

So far, there is nothing to account for the differing OCP curves of silicon between charging and discharging. Ai et al. (2022) used a sigmoid function to switch between the two curves.

$$sigmiod(x) = \frac{1 + \sinh(x)}{2}$$

$$\begin{aligned}\phi_{si}(CSC_{si}) = {} & sigmoid\left(-\frac{100j_{si}}{Q}\right)\phi_{si}^{dch}(CSC_{si}) \\ & + sigmoid\left(\frac{100j_{si}}{Q}\right)\phi_{si}^{ch}(CSC_{si})\end{aligned} \qquad \text{Eq. 10}$$

Where Q is the charge capacity of the battery. The constant "100" is stated to be a tunable parameter which gave Ai et al. the best results.

A sample code was provided to the group. It was modified to take an input of a current cycle to simulate the output voltage. Due to the sign convention of the model, the current data is scaled by -1. The switching function of Equation was incorporated to the DAE function. The model was also modified to take parameters as inputs, so a particle swarm algorithm could be run to identify parameters.

SOH Indicator Parameters

Prasad and Rahn (2013) found that two parameters, estimated resistance and diffusive time constant, can potentially be used as SOH indicators. Figure 24 shows these parameters as identified by Prasad and Rahn. It shows that the estimated resistance, K_r of Equation 5, in red crosses and the diffusion time constant, τ, in green circles. These parameters increase monotonically with age, making them prime candidates for SOH indicators. It also shows the capacity factor in blue dots, but that parameter increases until 4000 cycles, then decreases. Since multiple SOH points can coincide with the same capacity factor, it cannot be used as an indicator.

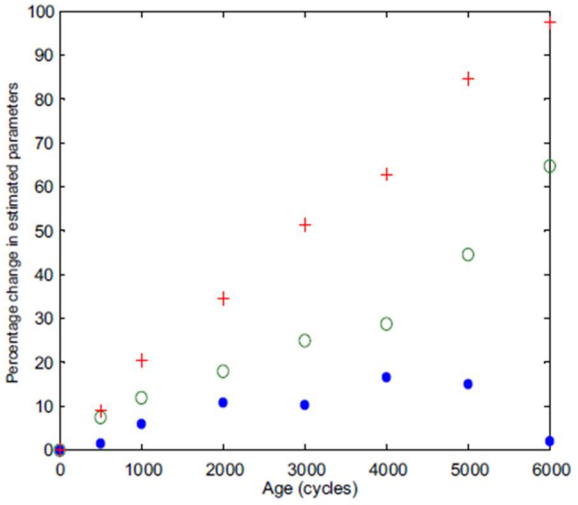

Fig. 5. Estimated resistance ($\hat{R}_T^+$, +), diffusion time ($\hat{\tau}_D^+$, o), and capacity factor ($\hat{C}^+$, •) versus age.

Figure 24: Estimated Resistance, Diffusion Time Constant, and Capacity Factor Identified by Prasad and Rahn (2013)

Couto et al. (2016, Part I) used this as motivation for their model to incorporate the diffusive time constant as a state with Kalman Filter for real time identification. In Part II of that research, Schorsch et al. (2016) verified its use, stating "the satisfactory results for the estimation of τ, it is expected that the proposed approach can be used to periodically access the battery SOH power fade" (p. 4034). However, both Prasad and Rahn and Couto/Schorsch et al. focused on single material electrodes. It is still unclear if the relationship still holds for composite material anodes.

Experimental Procedure

An LG-MJ1 cell with nominal voltage of 3.7 V and nominal capacity of 3400 mAh was placed in an Arbin cylindrical cell tester. A thermocouple was taped to the center of the cell to measure

temperature for other research by the group, but this does not affect the current and voltage measurements. The cells were cycled with 0.2C CC between cutoff voltages of 2.5 V and 4.2 V to check the capacity. They were then cycled 20 times with 1C CCCV at with cutoff current of 0.2C to induce aging. The cycling was repeated until the discharge capacity was less than 2.1 Ah (60% SOH).

The code was modified to take input data for current and voltage. The built-in function for particle swarm optimization was used in MATLAB to identify parameters of the 0.2 CC cycles at different SOH stages. The objective function was defined as the root mean square error (RMSE) between the simulated voltage and measured voltage.

$$RMSE = \sqrt{\frac{\sum_{t=1}^{N}\left(V_{meas}(t) - V_{sim}(t)\right)^2}{N}} \qquad \text{Eq. 11}$$

The particle swarm was set to identify the parameters charge transfer reaction rate k for cathode and anode; estimated resistance K_r; diffusive time constant τ for cathode, graphite, and silicon; maximum lithium concentration C_{max} for cathode, graphite, and silicon; and the amount of silicon in the anode. All other model parameters were found from available sources and are summarized in Table 8. The input data used was the 0.2C CC charge and discharge cycle from each SOH stage. Since each of these cycles had around 32000 data points, only every tenth data point was taken to save on runtime.

Table 8: Model Parameters Available from Literature – [A] Heenan et al. (2020) [B] Zhuo et al. (2023) [C] Schmitt et al. (2021)

Element Parameters	**Cathode**	**Separator**	**Anode**
Thickness L (μm)	85 [A]	12 [B]	72 [A]
Active Material Volume Fraction ϵ	0.64 [A]	0.7 [A]	0.02-0.03 [A]
Material Parameters	**Cathode**	**Graphite**	**Silicon**
Particle Radius R (μm)	3 [A]	7.5 [A]	1.5 [A]
Current Collector Area A (m^2)	0.071 [C]	0.071 [C]	0.071 [C]

Average Lithium Concentration in Electrolyte $\overline{C_e}$	1000 [B]	1000 [B]	1000 [B]

Another cell was also sampled to experiment with Urban Dynamometer Drive Schedule (UDDS) data to demonstrate model performance with dynamic charging profiles. A fresh cell was cycled with 0.2C CC, 0.5C CC, and 1C CC charge and discharge to collect data for parameter identification. Then, a UDDS data current schedule was used to simulate the battery cell as well as collect data on the Arbin tester.

Results and Discussion

The charge and discharge capacities during the 0.2C CC cycles are shown in Table 9. There was not an initial charge and discharge capacity taken with 0.2C CC at the beginning of cycling, so the SOH is based on the nominal capacity of the cell (3400 mAh).

Table 9: SOH of LG-MJ1 Cell While Cycling

Cycles	Charge Capacity (Ah)	Discharge Capacity (Ah)	SOH (%)
20	3.18	3.16	93.0
40	3.10	3.10	91.1
60	2.93	2.95	86.6
80	2.74	2.78	81.6
100	2.55	2.57	75.7
120	2.35	2.38	69.9

Model Accuracy

The best parameter sets obtained at each SOH for each set of input data are shown in Table 10. Table 11 shows the RMSE obtained using that set of parameters during the particle swarm optimization.

Table 10: Best Parameters Identified by Particle Swarm Algorithm

SOH %	k_n 10^{-6}	k_p 10^{-6}	K_r	τ_p	τ_{gr}	τ_{si}	$C_{max,si}$	$C_{max,n}$	$C_{max,pi}$	ϵ_{si}

93.0	1.57	0.13	2.36×10^{-7}	2500	3115	0.0947	140347	30903	58302	2.2%
91.1	2.67	3.86	0.0023	3500	2000	0.066	152791	25937	57740	2%
86.6	4.71	5.23	0.0048	3678	1496	2.12	148861	29493	60917	2%
81.6	49.1	0.14	0.0024	5408	2000	12.1	163582	27168	63781	2%
75.7	33.7	1.53	0.0061	6824	1000	65.3	190000	40000	58196	2%
69.9	13.3	2.59	0.0055	9999	1002	8.98	189953	39995	62690	2%

Table 11: Best RMSE Value from Particle Swarm at Various SOH Stages

SOH %	**93.0**	**91.1**	**86.6**	**81.6**	**75.7**	**69.9**
RMSE (mV)	12.71	11.70	21.11	33.17	106.6	104.6

The best RMSE was 11.70 at 91.1% SOH. As the cell aged, the best RMSE value increased, signifying that it may be harder to identify the parameters at later SOH stages or the search bounds were not set properly. Schmitt et al. (2021) found that for LG-MJ1 cells, the NMC811 of the cathode does not have an OCP curve that varies with age. They found that the anode, however, varied greatly with aging, possibly due to decreased contribution from the silicon material. Changes in the OCP curve were not accounted for in the model, which could account for some or all the high errors at later SOH stages. Another possibility is the loss of active material or loss of lithium inventory are not accounted, which could impact results.

To visually demonstrate the results of the model, the parameters identified at 93.0% SOH were simulated with the input data from 93.0% SOH. The following figures are the results.

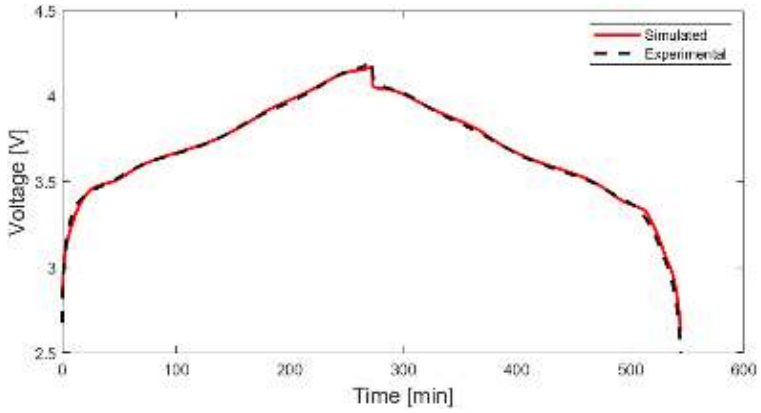

Figure 25: Plots of Simulated and Experimental Voltage vs Time at 93.0% SOH

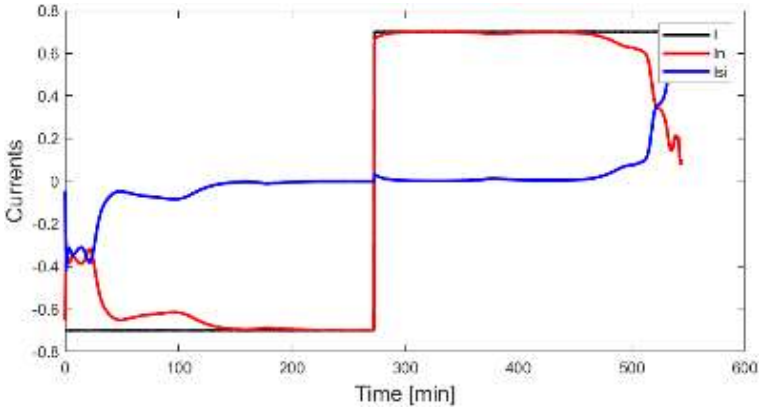

Figure 26: Current Contributions of Silicon and Graphite vs Time at 93.0% SOH

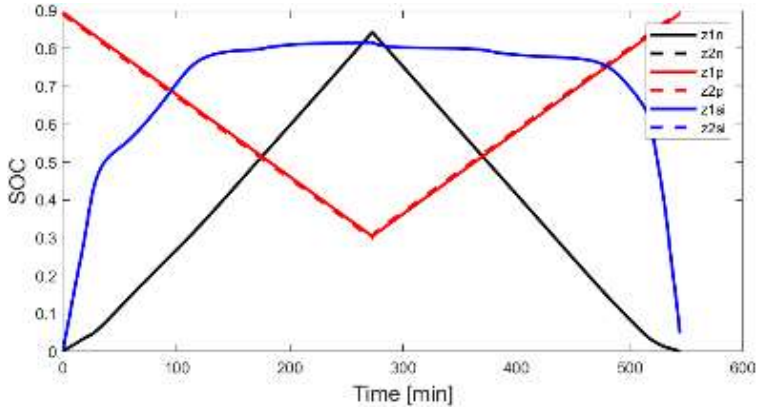

Figure 27: SOC of Graphite, Cathode, and Silicon vs Time at 93.0% SOH

Figure 25 shows the plots of voltage vs time for both the simulation results and experimental data. It used every data point from the charge cycle instead of every tenth data point, resulting in an RMSE of 17 mV compared to 12.7 mV. Figure 25 shows that the two lines are almost

identical, showing that the equivalent hydraulic model can be used to accurately predict the voltage given a current input and properly tuned parameters.

Figure 26 shows the total current input (I, in black), and the current contributions of graphite (n, in red) and silicon (Si, in blue). The contributions of silicon and graphite show some oscillation in the beginning, possibly due to the model converging to the proper states. When the cell is at low states of charge, approximately 0 to 50 minutes (charging) and 500 minutes to the end (discharging), the silicon contributes more current than graphite. This replicates the results by Ai et al. (2022), who found that "at high SOCs, the current density is mostly dominated by graphite and at low SOCs, the silicon starts to output the majority current density.

Figure 27 shows surface and bulk concentrations states of each component vs time. It shows the silicon (blue) rises steeply at the start of charging, flattens out in the middle of charging until towards the end of charging, then steeply drops. This again shows the high contribution from silicon at low SOC ranges. The cathode material changes linearly in its stoichiometric range, which is expected since there is only one material in the cathode.

A problem that is commonly encountered with parameter identification is "overfitting" the parameters to one data set such that it results in large errors when used in other data sets. To demonstrate any possible overfitting, the parameters identified at 93.0% SOH were simulated with cycles from 93.0% SOH to 91.1% SOH, using every tenth data point to reduce computation time. In this range, the battery degrades so there should be a change of parameters, which is verified by Table 10 above. If overfitting is an issue, this simulation would have high error. Another source of error in this data set that overfitting would impact is using a different charge cycle. The simulated data includes 20 cycles of 1C CCCV charge/discharge and 1 cycle of 0.2C CC charge/discharge. The RMSE over this range with the parameters from 93.0% was 35.5 mV. This is almost triple the error from the 0.2C CC cycle. Figure 28 shows the simulated and experimental voltage vs time.

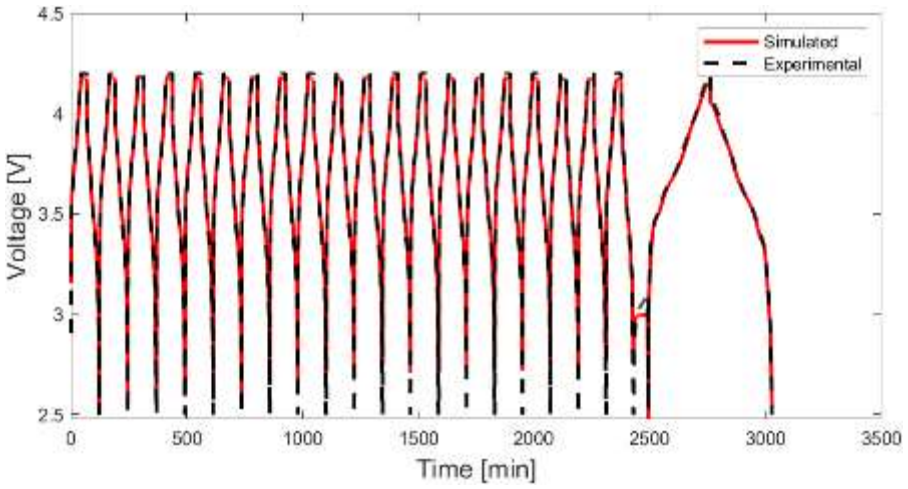

Figure 28: Plots of Simulated and Experimental Voltage vs Time from 93.0% to 91.1% SOH

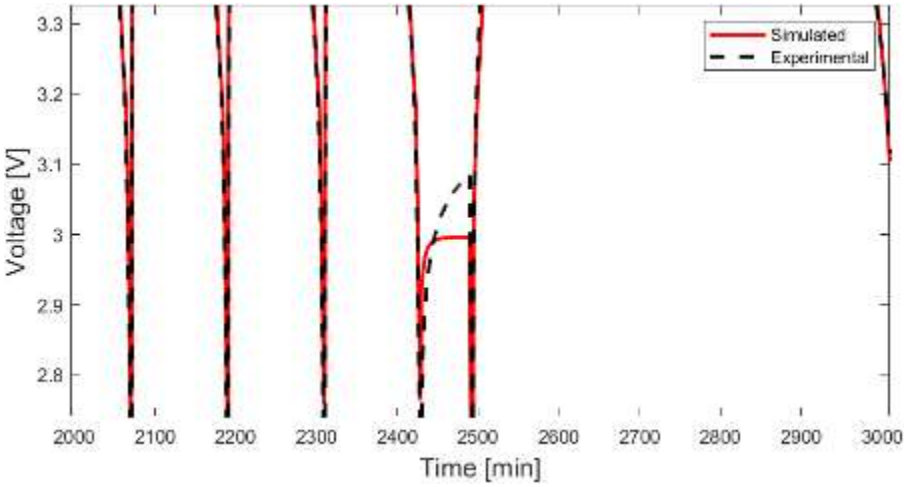

Figure 29: Zoomed In Plot Emphasizing Error from Figure 28

From Figure 28, there is a noticeable gap in the between the simulated and experimental data at 2500 min, or when the charge condition changes from 1C CCCV to 0.2C CC. There is also a resting phase in between these conditions where the current input is 0 A. The noticeable gap indicates there is high error in this region. Figure 29 zooms into this region to make it clearer how large the error is, up to around 100 mV. Besides this one region, the simulated and experimental voltages from the plots in Figure 28 align very well, signifying that overfitting is not an issue in this SOH range.

Table 12 shows the parameters identified for the LG-MJ1 cell that was used for UDDS charging. They resulted in an RMSE of 24.2 mV.

Table 12: Parameters Identified for New Cell for UDDS Cycling

SOH %	k_n 10^{-6}	k_p 10^{-6}	K_r	τ_p	τ_{gr}	τ_{si}	$C_{max,si}$	$C_{max,n}$	$C_{max,pi}$	ϵ_{si}
100	0.36	10.8	1.0E-06	4432	0.11	5161	166317	33084	60017	2.88 %

The above parameters were then used to simulate the UDDS schedule. The RMSE between the simulated and experimental voltage was 55.4 mV, which is very large compared to CC or CCCV simulations. However, in the UDDS part of the test, the RMSE was 23.5 mV. The simulated and experimental voltage vs time are shown in Figures 30 and 31.

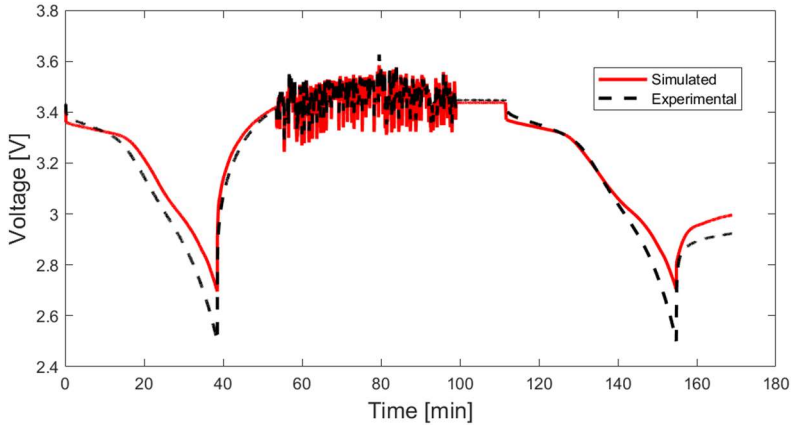

Figure 30: Plots of Simulated and Experimental Voltage vs Time with UDDS Cycle

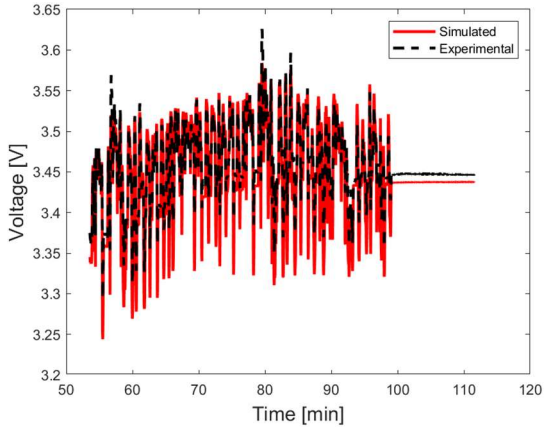

Figure 31: Plots of Simulated and Experimental Voltage vs Time Zoomed-In to UDDS Cycle

Figure 30 shows that there is a very large error in the 0.2 C CC charge before the UDDS cycle (this charge was to prevent the cell from being over discharged during the UDDS cycle). This points to needing better data that includes 0.2C CC charging and discharging, for parameter

identification. Though the error is not quite as large, Figure 31 shows that the UDDS cycling sees greater error when the current is suddenly changed from charging to discharging. It is hard to say for certain without better parameters being identified, but a possible explanation is that this cell was at a low SOC (approximately 5%). At low SOCs, silicon contributes the majority of the current. This could amplify any effect caused by the hysteresis between silicon's charge and discharge curves, since the silicon is switching between the curves during the UDDS cycle. More work will be done to simulate the UDDS at different SOC ranges to determine if poor parameter identification is causing the error or if switching between the OCP curves with Equation 10 is causing the error.

SOH Estimation

Table 13: Best SOH Identifying Parameters Identified at Different SOH Stages

SOH %	K_r	τ_p	τ_{gr}	τ_{si}	RMSE
93	2.36×10^{-7}	2500	3115	0.0947	12.71
91.1	1.88×10^{-6}	3999	1500	0.002	11.51
86.6	0.0048	3680	1496	2.12	21.11
81.6	0.006	4026	2000	1.25	30.4
75.7	0.0061	6824	1000	65.3	106.6
69.9	0.0055	9999	1002	8.98	104.6

Table 13 shows the best identified SOH indicating parameters at each SOH stage. The estimated resistance K_r, diffusive time constant of the cathode τ_p, and diffusive time constant of the silicon τ_{si} all increase with aging. However, the high RMSE at later stages questions the accuracy of the identified parameters.

To ensure the validity of the SOH indicating parameters, the particle swarm algorithm was run five times at the SOH stages of 93.0%, 91.1%, 86.6%, and 81.6%. This was not done at 75.7% and 69.9% since 80% SOH is typically when batteries are replaced. The estimated resistance and diffusive time constants from the three parameter sets with the lowest RMSE were averaged and graphed. Figure 32 shows the graph of these parameters vs SOH stage. Note that the SOH decreases along the x-axis. Table 15 shows the average diffusive time constant and estimated resistance parameters at each SOH stage, as well as the standard deviation.

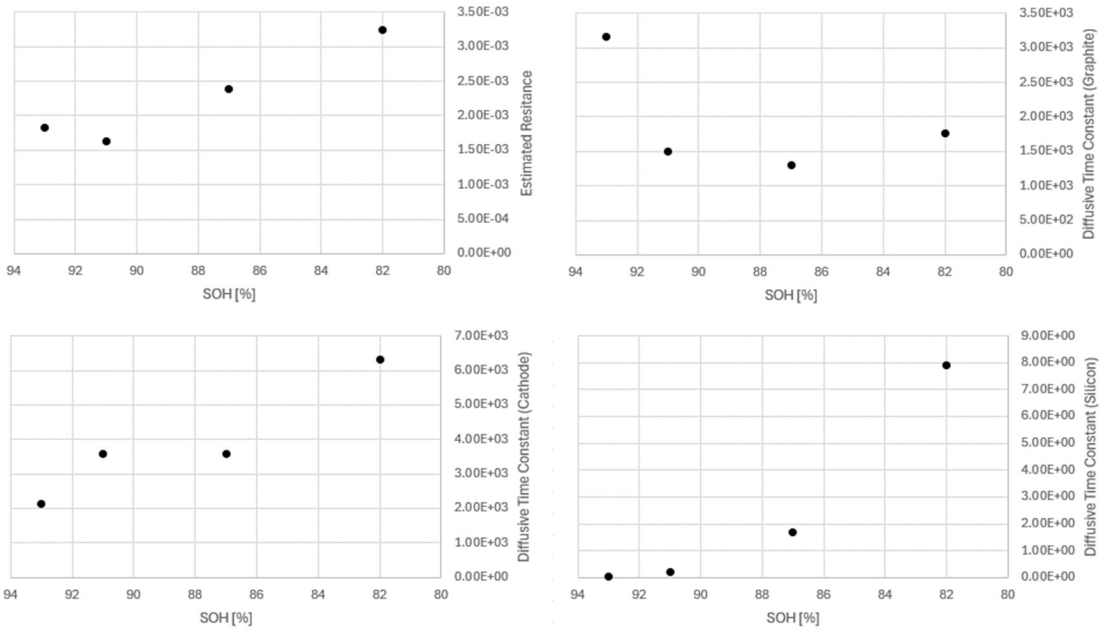

Figure 32: Average Identified Parameters vs SOH for [Top Left] Estimated Resistance and Diffusive Time Constants of [Top Right] Graphite [Bottom Left] Cathode and [Bottom Right] Silicon

Table 14: Averages and Standard Deviation of Identified Parameters

SOH	K_r		τ_p		τ_{gr}		τ_{si}	
%	Avg.	St. Dev.	Avg.	St. Dev.	Avg.	St. Dev.	Avg.	St. Dev.
93.0	0.00182	0.0017	2126	330	3159	167	0.045	0.043
91.1	0.00163	0.0014	3570	399	1501	499	0.202	0.292
86.6	0.00239	0.0023	3569	569	1307	214	1.682	0.609
81.6	0.0032	0.0007	6315	1936	1760	417	7.903	5.530

Figure 32 and Table 14 show that the estimated resistance decreases from 93.0% to 91.1% SOH, then increases with aging. The diffusive time constant for the graphite decreases until 86.6% SOH then increases. The diffusive time constant for the cathode increases from 93.0% to 91.1% SOH, remains the same at 86.6% SOH, then increases again. The diffusive time constant for the silicon increases with aging for all data points. From this, the best potential SOH indicator is the diffusive time constant for silicon and estimated resistance and diffusive time constant for graphite cannot be used as SOH indicators. However, Table 14 shows that the standard deviation is large, relative to the average, for all parameters at all stages. This indicates high variability amongst the identified parameters. More work is needed in finding the true parameters of the model, whether that is model based or experimental methods, before concluding which SOH indicators are best in a LG-MJ1 silicon-graphite anode cell.

Follow-On Work

The area the EHM struggles the most is producing reliable results from the parameter identification. Zhuo et al. (2023) compiled model parameters for the LG-MJ1 from manufacturer specifications, prior research, or calculations. However, they have parameters for the combined anode (not silicon and graphite individually). This makes it difficult to confirm impactful parameters, especially those in the anode. If these parameters cannot be found, then they should be investigated in the future. This can include different experimental techniques or creating a DFN or SPM model and comparing results. After this, a more reliable relationship between identified parameters and SOH can be determined. Additional follow-on work can include parameter identifiability analysis to determine if unique parameter sets can be identified.

Conclusion

An equivalent hydraulic model was created to model a silicon-graphite anode battery (LG-MJ1 cells). The silicon and graphite were modeled as being in parallel, creating a system of DAEs. Particle swarm optimization was used to identify parameters used in the model. At 91.1% SOH, the RMSE between the simulation voltage and experimental voltage reached as low as 11.7 mV, but the error was much higher at lower SOH (104.6 mV at 69.9% SOH). Potential causes for the greater error at lower SOH ranges could be do to changing OCP curves or poor bounds used in parameter identification.

The model was able to accurately capture the dynamics of silicon and graphite, replicating the high silicon contribution at low SOC and high graphite contribution in higher SOC ranges. The model was also able to simulate different cycling types (0.2 CC vs 1C CCCV) across the SOH range of 93.0% to 91.1% with only a slight increase in error likely due to a resting phase.

A UDDS current schedule was used to simulate another battery cell at a low SOC range, where the current contribution of silicon is the greatest. There was a large error during the 0.2C CC charging phase before the UDDS phase, most likely due to using poor data for parameter identification. The model was able to simulate the UDDS cycle but had encountered greater error when the current rapidly switched from charging to discharging or vice versa. More work is needed to determine if the error is due to model insufficiency or poor parameter identification. More work is needed for simulating a UDDS cycle in different SOC ranges.

The best parameter found for SOH indication is the diffusive time constant of silicon. The diffusive time constant of the cathode also should potentially promising results. However, due to high standard deviation/variance of the identified estimated resistance, it cannot be confirmed which parameters may be best, or usable, in a composite anode battery.

Summary of Both Investigations

Two different state of health estimation approaches were presented in this work. The first approach was experimental, using 3D DIC technology to measure z-displacement, or thickness. The second approach was model-driven, using an electrochemical based equivalent hydraulic model.

In the experimental approach, the 3D DIC data showed there was limited hysteresis between charging and discharging, reducing the amount of required data for practical state of health estimating. It was determined that there is a strong linear correlation between the state of health of a battery and its z-displacement at 0% state of charge. The data showed a parabolic relationship between z-displacement and voltage at different state of health stages. This suggests that given a displacement measurement and voltage, it may be possible to predict the state of health. More work is needed to confirm this hypothesis. The points that best represented the average displacement were at the center or along the long sides.

In the model-driven approach, an equivalent hydraulic model was modified to take current inputs to simulate voltage. Parameters were identified using particle swarm in MATLAB with real current and voltage measurements. Using identified parameters, the model could accurately simulate simple charge and discharge cycles, i.e. CC and CCCV, at higher states of health. At lower states of health, the model encountered much greater error, possibly due to changing OCP curves in the anode.

A UDDS current profile was simulated with parameters identified from 0.5C and 1C CC charging cycles, resulting in large error during the 0.2C CC before the UDDS. During the UDDS cycling, the largest simulated voltage error was when the current rapidly switched from charging to discharging. This could be due to either poorly identified parameters or the method used for capturing the differing charge and discharging OCP curves of silicon (a sigmoid function). More work is needed in parameter identification for use in UDDS cycling before determining if another method is needed for capturing the hysteresis between the charge and discharge OCP curves of silicon.

Potential state of health indicating parameters, diffusive time constant of each material and estimated resistance, were identified at different states of health. The identified parameters showed the diffusive time constant of silicon increased with aging. The diffusive time constant of

silicon may be promising for estimating the SOH of the silicon-graphite composite anode battery. The diffusive time constant of the cathode also tended to increase with aging. The estimated resistance and diffusive time constant of graphite did not continually increase with aging, so they may not be reliable SOH indicators. However, there was high variability of the identified parameters, so no absolute conclusion can be drawn yet. Better parameter identification is needed in future work.

References

Auto Trader. (2023, September 7). Fewer than half of drivers willing to make electric vehicle switch – Auto Trader. In *Press Releases.* Retrieved from Auto Trader website: https://plc.autotrader.co.uk/news-views/press-releases/fewer-than-half-of-drivers-willing-to-make-electric-vehicle-switch-auto-trader/

Edge, J.S., O'Kane, S., Prosser, R., Kirkaldy, N.D., Patel, A.N., Hales, A., Ghosh, A., Ai, W., Chen, J., Yang, J., Li, S., Pang, M., Diaz, L.B., Tomaszewska, A., Marzook, M.W., Radhakrishnan, K.N., Wang, H., Patel, Y., Wu, B., & Offer, G.J. (2021). Lithium ion battery degradation: What you need to know. *Physical Chemistry Chemical Physics, 23,* 8200-8221. https://doi.org/10.1039/D1CP00359C

Leung, P.K., Moreno, C., Masters, I., Hazra, S., Conde, B., Mohamed, M.R., Dashwood, R.J., & Bhagat, R. (2014). Real-time displacement and strain mappings of lithium-ion batteries using three-dimensional digital image correlation. *Journal of Power Sources, 271*, 82-86. https://doi.org/10.1016/j.jpowsour.2014.07.184

Kwon, H.J., Hwang, J.Y., Shin, H.J., Jeong, M.G., Chung, K.Y., Sun, Y.K., & Jung, H.G. (2020). Nano/Microstructured silicon−carbon hybrid composite particles fabricated with corn starch biowaste as anode materials for Li-Ion batteries. *Nano Letters*, *20*(1), 625-635. https://pubs.acs.org/doi/10.1021/acs.nanolett.9b04395

Ai, W., Kirkaldy, N., Jiang, Y., Offer, G., Wang, H., & Wu, B. (2022). A composite electrode model for lithium-ion batteries with silicon/graphite negative electrodes. *Journal of Power Sources*, *527*(231142). https://doi.org/10.1016/j.jpowsour.2022.231142

Mohtat, P., Lee, S., Siegel, J.B., & Stefanopoulou, A.G. (2019). Towards better estimability of electrode-specific state of health: Decoding the cell expansion. *Journal of Power Sources, 427*, 101-11. https://doi.org/10.1016/j.jpowsour.2019.03.104

Szalai, S., Szürke, S.K., Harangozó, D., & Fischer, S. (2022). Investigation of deformations of a lithium polymer cell using the Digital Image Correlation Method (DICM). *Reports in Mechanical Engineering, 3*(1). https://doi.org/10.31181/rme20008022022s

Zhuo, M., Offer, G., & Marinescu, M. (2023). Degradation model of high-nickel positive electrodes and cyclable lithium on capacity fade. *Journal of Power Sources, 556*. https://doi.org/10.1016/j.jpowsour.2022.232461

Royal Society of Chemistry. (2024). Uses and properties: Natural abundance. In Periodic Table: Silicon. Retrieved from Royal Society of Chemistry website: https://www.rsc.org/periodic-table

Zhu, G., Yang, S., Wang, Y., Qu, Q., & Zheng, H. (2019). Dimethylacrylamide, a novel electrolyte additive, can improve the electrochemical performances of silicon anodes in lithium-ion batteries. *Royal Society of Chemistry*, *9*, 435-443. DOI: 10.1039/c8ra07988a

Adham, S., Jackson, M., Durant, C., & Laugharne, A. (2023, February 15). *Navigating the rapidly evolving EV battery chemistry mix.* Retrieved from CRU Group website: https://www.crugroup.com/knowledge-and-insights/insights/2023/navigating-the-rapidly-evolving-ev-battery-chemistry-mix/

Xia, L., Najafi, E., & Donkers, M.C.F. (2017). A computationally efficient implementation of an electrochemistry-based model for lithium-ion batteries. *IFAC (International Federation of Automatic Controls) PapersOnLine,* 50(1), 2169-2174. https://doi.org/10.1016/j.ifacol.2017.08.276

Moura, S.J., Argomedo, F.B., Klein, R., Mirtabatabaei, A., & Krstic, M. (2017). Battery state estimation for a single particle model with electrolyte dynamics. *IEEE Transactions on Control Systems Technology, 25*(2), 453-468. DOI: 10.1109/TCST.2016.2571663

Zülke, A., Korotkin, I., Foster, J.M., Nagarathinam, M., Hoster, H., & Richardson, G. (2021). Parametrisation and use of a predictive DFN model for a high- energy NCA/Gr-SiOx battery. *Journal of The Electrochemical Society, 128*(12). DOI 10.1149/1945-7111/ac3e4a

Goldar, A., Romagnoli, R., Couto, L.D., Romero, A., Kinnaert, M., & Garone, E. (2020). MPC strategies based on the equivalent hydraulic model for the fast charge of commercial Li-ion batteries. *Computers and Chemical Engineering, 141*. https://doi.org/10.1016/j.compchemeng.2020.107010

Mu, D., Jiang, J., & Zhang, C. (2013). Online semiparametric identification of lithium-ion batteries using the wavelet-based partially linear battery model. *Energies, 6*(5), 2583-2604. DOI:10.3390/en6052583

Couto, L.D., Schorsch, J., Nicotra, M.M., & Kinneart, M. (2016). SOC and SOH estimation for Li-ion batteries based on an equivalent hydraulic model. Part I: SOC and surface concentration estimation. *2016 American Control Conference*, 4022-4028. DOI:10.1109/ACC.2016.7525553.

Gao, Y., Sun, Z., Zhang, D., Shi, D., & Zhang, X. (2023). Determination of half-cell open-circuit potential curve of silicon-graphite in a physics-based model for lithium-ion batteries. *Applied Energy, 349*. https://doi.org/10.1016/j.apenergy.2023.121621

Prasad, G.K. and Rahn, C.D. (2013). Model based identification of aging parameters in lithium ion batteries. *Journal of Power Sources, 232*, 79-85. https://doi.org/10.1016/j.jpowsour.2013.01.041

Speltino, C., Stefanopoulou, A.G., & Fiengo, G. (2013). Parametrisation and estimation of surrogate critical surface concentration in lithium-ion batteries. *International Journal of Vehicle Design, 61(*1/2/3/4), 128-156. DOI:10.1504/IJVD.2013.050843

Bartlett, A., Marcicki, J., Onori, S., Rizzoni, G., Yang, X.G., & Miller, T. (2016). Electrochemical model-based state of charge and capacity estimation for a composite electrode lithium-ion battery. *IEEE Transactions on Control Systems Technology, 24*(2), 384-399. DOI: 10.1109/TCST.2015.2446947

Schorsch, J., Couto, L.D., & Kinnaert, M. (2016). SOC and SOH estimation for Li-ion battery based on an equivalent hydraulic model. Part II: SOH power fade estimation. *2016 American Control Conference,* 4029-4034. DOI: 10.1109/ACC.2016.7525554.

Heenan, T.M.M., Jnawali, A., Kok, M.D.R., Tranter, T.G., Tan, C., Dimitrijevic, A., Jervis, R., Brett, D.J.L., & Shearing, P.R. (2020). An advanced microstructural and electrochemical datasheet on 18650 Li-ion batteries with nickel-rich NMC811 cathodes and graphite-silicon anodes. *Journal of The Electrochemical Society*, 167(14). DOI:10.1149/1945-7111/abc4c1

Zhuo, M., Offer, G., & Marinescu, M. (2023). Degradation model of high-nickel positive electrodes: Effects of loss of active material and cyclable lithium on capacity fade. *Journal of Power Sources, 556*. https://doi.org/10.1016/j.jpowsour.2022.232461

Schmitt, J., Schindler, M., & Jossen, A. (2021). Change in the half-cell open-circuit potential curves of silicon-graphite and nickel-rich lithium nickel manganese cobalt oxide during cycle aging. *Journal of Power Sources, 556*. https://doi.org/10.1016/j.jpowsour.2021.230240.